Alkali trace elements in Gale crater, Mars, with ChemCam: Calibration update and geological implications

V. Payré, C. Fabre, A. Cousin, V. Sautter, R. Wiens, O. Forni, O. Gasnault, N. Mangold, P.-Y. Meslin, J. Lasue, et al.

AGU PUBLICATIONS

JGR

Journal of Geophysical Research: Planets

RESEARCH ARTICLE

10.1002/2016JE005201

Key Points:
- Revised Li, Sr, Rb, and Ba abundances have been obtained with updated univariate calibrations
- The trace element abundances of alkaline and magnesian rocks are similar to the composition of monzonitic and basaltic clasts in NWA7533
- Alkali trace element enrichments are associated with K-bearing minerals such as alkali feldspars, K-phyllosilicates, and probably micas

Supporting Information:
- Table S1

Correspondence to:
V. Payré,
valerie.payre@univ-lorraine.fr

Citation:
Payré, V., et al. (2017), Alkali trace elements in Gale crater, Mars, with ChemCam: Calibration update and geological implications, *J. Geophys. Res. Planets*, *122*, 650–679, doi:10.1002/2016JE005201.

Received 21 OCT 2016
Accepted 9 MAR 2017
Accepted article online 20 MAR 2017
Published online 30 MAR 2017

Alkali trace elements in Gale crater, Mars, with ChemCam: Calibration update and geological implications

V. Payré[1], C. Fabre[1], A. Cousin[2], V. Sautter[3], R. C. Wiens[4], O. Forni[2], O. Gasnault[2], N. Mangold[5], P.-Y. Meslin[2], J. Lasue[2], A. Ollila[4], W. Rapin[2], S. Maurice[2], M. Nachon[6], L. Le Deit[5], N. Lanza[4], and S. Clegg[4]

[1]GeoRessources, Université de Lorraine, Nancy, France, [2]Institut de Recherche en Astrophysique et Planétologie, Université Paul Sabatier-OMP/CNRS, Toulouse, France, [3]LMCM, Muséum d'Histoire Naturelle, Paris, France, [4]Los Alamos National Laboratory, Los Alamos, New Mexico, USA, [5]Laboratoire de Planétologie et Géodynamique, LPG-Nantes, Nantes, France, [6]Earth and Planetary Sciences, University of California, Davis, California, USA

Abstract The Chemistry Camera (ChemCam) instrument onboard Curiosity can detect minor and trace elements such as lithium, strontium, rubidium, and barium. Their abundances can provide some insights about Mars' magmatic history and sedimentary processes. We focus on developing new quantitative models for these elements by using a new laboratory database (more than 400 samples) that displays diverse compositions that are more relevant for Gale crater than the previous ChemCam database. These models are based on univariate calibration curves. For each element, the best model is selected depending on the results obtained by using the ChemCam calibration targets onboard Curiosity. New quantifications of Li, Sr, Rb, and Ba in Gale samples have been obtained for the first 1000 Martian days. Comparing these data in alkaline and magnesian rocks with the felsic and mafic clasts from the Martian meteorite NWA7533—from approximately the same geologic period—we observe a similar behavior: Sr, Rb, and Ba are more concentrated in soluble- and incompatible-element-rich mineral phases (Si, Al, and alkali-rich). Correlations between these trace elements and potassium in materials analyzed by ChemCam reveal a strong affinity with K-bearing phases such as feldspars, K-phyllosilicates, and potentially micas in igneous and sedimentary rocks. However, lithium is found in comparable abundances in alkali-rich and magnesium-rich Gale rocks. This very soluble element can be associated with both alkali and Mg-Fe phases such as pyroxene and feldspar. These observations of Li, Sr, Rb, and Ba mineralogical associations highlight their substitution with potassium and their incompatibility in magmatic melts.

1. Introduction

1.1. Mars Science Laboratory Overview and ChemCam Results

The Curiosity rover that landed in Gale crater in August 2012 is equipped with a variety of instruments to investigate the surface of Mars. The main goal of the Mars Science Laboratory mission (MSL) is to study the geology and the atmosphere in Gale crater to look for habitable environments. The landing site, called Bradbury Landing, is located at the distal end of alluvial fans at the outlet of a fluvial channel named Peace Vallis [*Palucis et al.*, 2014; *Grotzinger et al.*, 2015]. After landing, Curiosity traveled toward Yellowknife Bay, an area characterized by fine-grained sedimentary rocks (sols 55–325). The first igneous rocks enriched in alkali elements relative to the average Martian crust were found as floats on Bradbury Rise near the uppermost part of the Yellowknife Bay formation [*Stolper et al.*, 2013; *Sautter et al.*, 2015]. Then, Curiosity explored waypoints named Cooperstown and Kimberley from sols 550 to 636, where K-rich sedimentary rocks were also encountered [*Le Deit et al.*, 2016]. From the landing site, the rover drove ~9 km before reaching the Pahrump Hills outcrop (sols 750–940), which was the first encounter with material belonging to the base of Mount Sharp, formally known as Aeolus Mons.

Two emission spectroscopy instruments on the rover analyze the chemical composition of rocks and soils: the Chemistry Camera (ChemCam) and the Alpha-Particle X-ray Spectrometer (APXS) [*Campbell*, 2012]. Major, minor, and trace elements are quantified by both instruments. ChemCam consists of two subsystems: a laser induced breakdown spectroscopy instrument (LIBS) able to detect and analyze major and minor element compositions [*Wiens et al.*, 2012; *Maurice et al.*, 2012, 2016] and a high-resolution Remote Micro-Imager (RMI) with a resolution of 40 μrad and a field of view of 20 mrad. This RMI gives context imaging to the chemical analyses performed by LIBS [*Le Mouélic et al.*, 2015]. By acquiring light-induced emission, the

LIBS is able to analyze elemental compositions of rocks and soils at distances from 1.5 to 7 m [*Wiens et al*., 2012; *Maurice et al*., 2016]. Thirty laser shots are usually performed to investigate a given point. Each target is analyzed by 5 to 25 observation points. In addition to the major elements, many minor and trace element detections were reported such as Li, Sr, Ba, and Rb [*Ollila et al*., 2014; *Fabre et al*., 2014]. As ChemCam is the first LIBS instrument developed and used on another planet, a careful calibration technique is needed [*Wiens et al*., 2013; *Clegg et al*., 2017].

In this paper, we broaden the calibration and the investigation of trace elements for Li, Rb, Sr, and Ba first studied by *Ollila et al*. [2014]. Indeed, for calibrations, this earlier study used a laboratory database containing 66 standards that did not adequately cover the compositional ranges that have been encountered in Gale crater. As a result, *Clegg et al*. [2017] expanded and updated this database to ~400 diversified standards with a larger range of concentrations, which was used to better quantify the major elements. Here univariate calibration models are used on these new data to better constrain the quantification of Li, Rb, Sr, and Ba compositions obtained during the first 1000 sols (Martian days). We discuss possible igneous and/or alteration processes that could explain elevated trace element contents in comparison with most of Gale crater materials. Finally, we broaden the discussion by comparing the distribution of Li, Sr, Rb, and Ba concentrations in Gale crater with their compositions in Martian meteorites, including the breccia NWA 7533.

1.2. Laser Induced Breakdown Spectroscopy (LIBS)

ChemCam uses a pulsed laser to ablate nanogram to microgram quantities of geological samples at distances varying from 1.56 to 7 m and then collects the light emitted by the deexcitation of ions, atoms, and molecular species constituting the plasma generated by the laser ablation of the target. These emissions occur at characteristic wavelengths which ChemCam records from the ultraviolet to the visible and near infrared [*Maurice et al*., 2012; *Wiens et al*., 2012]. The laser system generating the beam produces a focused spot on targets with a diameter between 350 and 550 μm [*Maurice et al*., 2012]. This enables us to analyze nearly pure minerals when they are larger than the spot size. This aspect is described in section 4. The light is received by a 110 mm diameter telescope on the mast of the rover. It is focused into an optical fiber which transports the signal to a demultiplexer and three spectrometers covering 240–850 nm [*Wiens et al*., 2012], located in the body of the rover. The emitted photon energies are analyzed by spectrometry to determine the elemental composition of the target (for reviews of LIBS, in general, see *Cremers and Radziemski* [2006] and *Miziolek et al*. [2006 and references therein]). Each ChemCam target is observed by using a raster pattern (the most used are 1×5, 1×10, and 3×3) to obtain a better sampling of the bulk rock and to observe the compositional variability of a target. ChemCam is sensitive to many chemical elements and is used to detect or quantify the concentrations of all major elements (Si, Ti, Al, Fe, Mg, Ca, Na, and K [*Wiens et al*., 2013; *Clegg et al*., 2017]) and a large set of minor and trace elements such as H [*Schröder et al*., 2015; *Rapin et al*., 2016]; C [*Beck et al*., 2016]; P, S, and Ni [*Forni et al*., 2015; *Nachon et al*., 2014, 2016; *Meslin et al*., 2016]; Cl [*Meslin et al*., 2016]; Li, Sr, Ba, and Rb [*Ollila et al*., 2014; *Fabre et al*., 2014]; Mn [*Lanza et al*., 2015, 2016]; F [*Forni et al*., 2015; *Meslin et al*., 2016]; Zn [*Lasue et al*., 2016]; Cu [*Payré et al*., 2016]; and N and Cr. Most of these elements are also discussed in *Wiens et al*. [2015] and *Maurice et al*. [2016]. For most elements there are many LIBS emission lines. Considering an optically thin plasma, the emission line (peak) intensity is often a linear function of the element concentration. Yet self-absorption can occur in particular cases like in a thick plasma with high density or depending on the nature of the matrix analyzed: outer layers of plasma absorb photons emitted by the central portion of the plasma. In such cases, the curves of the peak intensity versus the element concentration exhibit saturation [*Ollila et al*., 2014]. The RMI provides geological context images and documents the accurate location of each LIBS pit. This is the highest-resolution remote imager on Curiosity, identifying 0.4 mm features from a 10 m distance [*Maurice et al*., 2016; *Le Mouélic et al*., 2015].

Ollila et al. [2014] and *Fabre et al*. [2014] have already used different analysis techniques (univariate and multivariate partial least squares models) on ChemCam LIBS spectra to quantify data from Li, Sr, Rb, and Ba. These trace element calibration curves, down to several ppm, were used as a rapid tool to identify anomalous materials along the traverse. In this study, we update the Li, Sr, Rb, and Ba calibrations performed by *Ollila et al*. [2014] using a new laboratory database containing a wider diversity of geological samples, with ranges of concentrations that better represent the chemical diversity at Gale crater on Mars [*Clegg et al*., 2017].

1.3. Terrestrial Geological Occurrences of Li, Sr, Rb, and Ba

Lithium, strontium, rubidium, and barium concentrations are helpful to understand the geological processes that have acted on the materials under study. In igneous materials, Li occurs predominantly in silicate minerals and is widely present as an accessory element in K-feldspars, micas, and lepidolites, where it can substitute for Na, K, and Mg. During magmatic processes Li^{2+} can replace Fe^{2+} and Mg^{2+} in pyroxenes [*Ure and Berrow*, 1982]. Strontium may substitute for Ca and K in minerals in midstage melt differentiation. As a result, elevated Sr abundances are mostly found in intermediate rocks rather than in evolved igneous rocks. Strontium is mainly associated with K-feldspars, plagioclases, and fluorapatites where it can substitute for calcium [*Elliott*, 1994; *Deer et al*., 2001]. Rubidium is an incompatible element that has a similar ionic radius to potassium. As a result, it is mostly associated with potassic magmatic phases found in late stage of differentiation: micas and K-feldspar [*Deer et al*., 2001]. As the Ba^{2+} ion has a size close to K^{+} radius (as well as Rb), it is able to substitute for K within felsic minerals like alkali feldspars and micas [*Deer et al*., 2001]. This element is also a major component of Ba-hydroxylapatite. Note that apatite is a ubiquitous accessory mineral found within both mafic and felsic igneous rocks.

In sedimentary rocks, Li can be liberated especially at low pH levels by the weathering of secondary clay minerals [*Lyons and Welch*, 1997]. However, lithium-fluoride and lithium-phosphate compounds easily form, and due to their low solubility, Li becomes relatively immobile [*Stubblefield and Bach*, 1972]. In addition, lithium can be significantly adsorbed by clays such as illite. Li also occurs in mica alteration products and Mg-amorphous materials where it can substitute for Mg and Al. Strontium is strongly mobilized during weathering, especially in oxidizing acid environments, and is incorporated in clay minerals. Moreover, Sr^{2+} can replace Ca^{2+} in feldspars, carbonate minerals, and in sulfate and phosphate minerals (Ca-sulfate and Ca-phosphate). Additionally, Sr^{2+} can substitute for Ba^{2+} in sulfate minerals such as barite ($BaSO_4$) [*Simmons*, 1999]. Yet elevated amounts of strontium are mainly related to feldspar within alkaline rocks. Rubidium is mainly present in arkosic and feldspathic sandstones. In addition, during weathering, Rb is easily sorbed at high pH on potassic clay minerals like illite [*Heier and Billings*, 1970]. As a result, rubidium is mainly associated with potassic phases within alkali-rich rocks. Finally, similarly to rubidium, barium is mostly hosted within potassic minerals like K-feldspars and clay minerals, even though Ba shows a stronger affinity with feldspars rather than phyllosilicates [*Wedepohl*, 1978]. Moreover, barium abundances are depleted in sandstones and elevated amounts mainly indicate potassic materials [*Deer et al*., 2001]. During weathering, barium is easily sorbed by clay minerals and Fe-Mn-oxides [*Kabata and Pendias*, 2010].

These lithophile elements are in relatively high concentrations in alkaline igneous and sedimentary rocks, as well as in clay minerals. Many of these minerals and rocks were found by Curiosity at Gale crater on Mars. *Sautter et al*. [2015] and *Cousin et al*. [2017] described the observation of numerous felsic intrusive and volcanic materials in Gale, especially in the Hummocky plains, at the Bradbury landing site, and in the Kimberley formation. Potassic sandstones were encountered in Gale crater, especially at Kimberley [*Le Deit et al*., 2016], but also at Shaler [*Anderson et al*., 2015]. A number of pebble targets present a felsic composition [*Meslin et al*., 2013; *Cousin et al*., 2014]. *Léveillé et al*. [2014] described Mg-rich raised ridges enriched in clay minerals in Sheepbed mudstones in the Yellowknife Bay formation. Thus, relatively high Li, Sr, Rb, and Ba contents are to be expected in Gale crater. Quantification of these elements enables us to better constrain the potential minerals present within ChemCam targets and the environmental conditions that produced the inferred mineral phases.

2. Methods

2.1. New Laboratory Database

The original ChemCam calibration was done by using 66 pressed powder geochemical standards that were probed with the flight model before integration into the Curiosity rover [*Wiens et al*., 2013; *Ollila et al*., 2014]. *Ollila et al*. [2014] used this first version of the standard database, including the eight ChemCam Calibration Targets (CCCTs) [*Fabre et al*., 2011; *Vaniman et al*., 2012; *Wiens et al*., 2012] regularly analyzed with ChemCam on board the Curiosity rover. All other laboratory standards were pressed powder pellets consisting of material from igneous (63% of all data) and sedimentary (37%) rocks. However, this original database did not adequately cover all the compositional ranges that could be encountered in Gale crater. There are also significant gaps in the range of Li, Sr, Rb, and Ba concentrations in the calibration targets (CCCTs; Table 1).

Table 1. Trace Element Compositions in ppm in ChemCam Calibration Targets (CCCT) Onboard Curiosity Rover[a]

	Li (ppm)	Sr (ppm)	Ba (ppm)
Macusanite	3528	1.3	1.3
Norite	44	284	355
Picrite	7.2	1481	1283
Shergottite	7.5	654	1158
Kga-Med-S	7433	152	140
Nau2-Low-S	7433	236	162
Nau2-Med-S	7433	185	107
Nau2-High-S	7433	144	56

[a]*Fabre et al*. [2014] and *Vaniman et al*. [2012].

Thus, a larger diversity of standards with a large range of values was necessary to cover the Martian compositions and better constrain, among other elements, the abundances of strontium, lithium, barium, and rubidium. The details of their analyses and their compositions are described in *Clegg et al*. [2017].

The selected standards were chosen to cover the range of elemental abundances that are being encountered along Curiosity's traverse. The new laboratory database distribution used in this study for lithium, strontium, barium, and rubidium concentrations are shown in Figure 1. More than 400 standards were used including replicates of the eight CCCTs that mimic Martian rock compositions: synthetic glasses (shergottite, norite, and picrite), synthetic sulfate-bearing ceramics (from low to high sulfur content: NAU2-Lo-S, NAU2-Med-S, NAU2- Hi-S, and KGA-Med-S), and macusanite, a peraluminous obsidian glass [*Vaniman et al*., 2012; *Fabre et al*., 2011]. The new standards are mostly homogeneous pressed powder pellets with grain sizes usually smaller than 20–60 μm, and their compositions were analyzed by XRF and spectrometry including laser ablation- inductively coupled plasma-mass spectrometry (LA-ICP-MS) [*Wiens et al*., 2013; *Clegg et al*., 2017]. They are homogeneous at the laser beam scale. This database is used to calibrate the measurement of major and minor elements.

This set of standards covers a high diversity of rocks from various places: natural and synthetic sedimentary rocks (41.5% of standards), igneous rocks (43.5%), metamorphic rocks (5%), minerals (6.4%), evaporites, ores, and precipitate materials (3.4%). This new database is described in more detail in *Clegg et al*. [2017].

2.2. Experimental Setup

The spectra were obtained by using the Los Alamos National Laboratory (LANL) test bed which consists of the ChemCam engineering model mast unit (laser, telescope, imager, and associated electronics) and a laboratory copy of the body unit (optical demultiplexer, three spectrometers, electronics, and data processing unit), similar to the setup used by *Wiens et al*. [2013]. This test bed uses a Nd:KGW (neodymium-doped potassium gadolinium tungstate) pulsed laser providing an energy up to 14 mJ at 1067 nm on the target. The laser spot size on the target is smaller than 550 μm, and the light of the laser-induced plasma is collected by a coaxial telescope to be distributed to three spectrometers: ultraviolet (240.0–342.2 nm), violet (VIO; 382.1–469.3 nm), and visible to near infrared (VNIR; 473.7–906.5 nm) [*Maurice et al*., 2012; *Wiens et al*., 2012]. As optical differences exist between the flight and test bed models, instrument response functions (IRF) have been quantified [*Wiens et al*., 2012; *Clegg et al*., 2017]. The LIBS spectra recorded on Mars are thus multiplied by this IRF to produce calibrated spectra in photons. More technical details are available in *Wiens et al*. [2013] and *Clegg et al*. [2017].

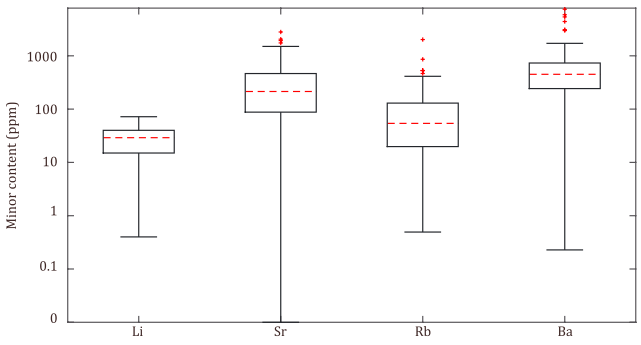

Figure 1. Boxplot of Li, Sr, Rb, and Ba concentration distribution within the laboratory database, described by *Clegg et al*. [2017]. The median is the dashed red line, the lower edge is the first quartile, and the upper edge is the third quartile. The lines on each side extend to the most extreme values except the outliers (red crosses).

For our investigation, the standards are placed into a vacuum chamber, which is pumped down and filled with 7 torr (933 Pa) CO_2, to simulate Martian pressure. For these calibrations, the laser source is placed 1.6 m away from the samples, where the flux is 1.5 GW/cm^2. Each standard is probed in five separate locations, and each location was probed with 50 laser shots to minimize any effects of heterogeneity in the sample.

This specific distance provides the possibility to compare between the ChemCam in-flight and the laboratory test bed using the onboard CCCTs in order to control the validity of the quantification.

2.3. Univariate Calibration

The trace element emission peaks with the greatest stability and the fewest interferences were previously identified by *Fabre et al*. [2014] for Li at 670.96 nm and Sr at 421.67 nm and by *Ollila et al*. [2014] for Rb at 780.2 nm and Ba at 455.53 nm. This is described in greater detail in section 3. For each sample of the new ground calibration database (section 2.1), five LIBS analyses were made on separate locations on each target, the 50 spectra at each location are averaged, then the average spectrum goes through the standard ChemCam data pipeline, including preprocessing and continuum subtraction, and Earth-to-Mars correction [*Wiens et al*., 2013]. These spectra are normalized to the spectral range; i.e., for each pixel the intensity is divided by the sum of the intensities of the studied peak spectral range [*Wiens et al*., 2013]. The selected emission lines of the five LIBS spectra processed for each sample are fitted with a Voigt function, and the long-baseline background is subtracted by a parabolic fit using an Interactive Data Language program. All possible overlapping lines are deconvoluted in order to minimize their interference with the studied elemental peaks. The integrated areas obtained from the selected lines are calculated and then ratioed to their composition in order to obtain a calibration curve for each element. Error bars shown in the calibration curves in Figures 3, 6, 9, and 11 represent the standard deviation calculated on the concentrations obtained by XRF and spectrometry measurements (on the *y* axis) and on the averages of the five areas obtained from the LIBS analysis (on the *x* axis).

In order to check the quality of each peak fitting, a fitting error is calculated for each sample spectrum (for each element) on a portion of n pixels. The error is determined by the sum of the square of the residuals between the real spectra (s_i) and the calculated Voigt function (v_i) for each pixel:

$$\text{fitting error} = \sum_{i=1}^{n} (s_i - v_i)^2$$

Several calibration equations can be deduced from these fittings. The accuracy of the univariate model is characterized by calculating the calibration error called the root-mean-square error (RMSE) of cross validation between the concentrations of the laboratory standards measured and the calculated predictions [*Wiens et al*., 2013; *Clegg et al*., 2017]. We usually consider that the model with the lowest RMSE is the most representative model. These predicted values are calculated by using the averaged area of a given line and by applying the equation of the calibration curve to obtain predicted abundances. The RMSE is the accuracy calculated by using the predicted and reference values for each standard of the training set. It is the square root of the sum of the square of the differences (d_i) between the predicted value (p_i) and the reference value (r_i) ($d_i = r_i - p_i$), divided by the number of the data points in the calibration (n):

$$\text{RMSE}\left[\left(\sum_{i=1}^{n} d_i^2\right)/n\right]^{1/2}$$

The estimates of the prediction error, the root-mean-square error predictions (RMSEP), have been calculated for Li, Sr, and Ba on the CCCTs on board the rover in order to verify the consistency between predictions and known values. We calculated the reliable limits of detection of the selected calibrations by using the 95% confidence bands method called LOD3 described in *Lasue et al*. [2012].

2.4. Previous Studies on Li, Sr, Rb, and Ba Calibrations

The LIBS technique is increasingly used for a variety of applications on Earth. Numerous papers present different types of calibration for trace elements including Li, Sr, Rb, and Ba for diverse applications with geological, environmental, biological, or medical goals. The following subsection discusses some relevant examples. Note that the presented applications were performed by using a different experimental setup from ChemCam and cannot be applied to Martian data.

2.4.1. Terrestrial LIBS Applications for Trace Element Quantification

Lithium calibration using LIBS has been developed by several studies. *Fabre et al*. [2002] calibrated lithium with a 266 nm neodymium: yttrium/aluminum/garnet (Nd:YAG) laser by using univariate calibration on Li I 670.7 nm, an unresolved doublet, in several natural minerals and synthetic glasses in a constant argon

atmosphere. Two distinct linear relationships between line intensity and Li concentration have been observed, one up to 0.3% and the other one between 0.3% and 8.5%. *Sweetapple and Tassios* [2015] used LIBS in ambient indoor atmospheric conditions to calibrate lithium. Their model was based on univariate calibration on the Li I 812.644 nm line. In order to deal with the physical and chemical matrix effects [*Hark and Harmon*, 2014], they used two different suites of samples: a series of synthetic silicate glass standards up to LiO_2 = 13.5 wt % and a series of six lithium-bearing rock and mineral standards pressed as pellets with LiO_2 up to 5.5 wt %. Synthetic glass calibration used a second-order polynomial function and displayed a large degree of self-absorption for lithium at high concentrations, while a linear curve was more appropriate for pressed pellet calibration. This self-absorption is clearly due to the absorption of emission from lithium in the hotter part of the plasma by lithium in the cooler part of the plasma. They observed that polynomial functions estimate lithium better in the two kinds of matrix.

Strontium abundances in solid materials have been studied in several papers. *Mansoori et al*. [2011] analyzed the Sr composition of cement powders by using Sr II 407.77 nm line to build a univariate calibration curve by using the ratio of the Sr line to the Ca II 306.85 nm line. They estimated a limit of detection (LOD) of 20.3 ppm. *Martin et al*. [2012] studied $CaCO_3$ pellets doped with strontium to calibrate the Sr I 460.8 nm line with a univariate model. They also tested multivariate analysis on the full spectrum. Their LOD was even lower, at 10 ppm.

Finally, barium has been studied by *Essington et al*. [2009]. They calibrated barium with univariate models on the 455.5, 493.4, and 553.55 nm lines. They observed that the best line to quantify Ba content is the 493.4 nm peak based on a strong correlation between peak area and barium concentration and a low relative error of prediction. *Eppler et al*. [1996] used doped sand and soils to calibrate the Ba 233.5 nm line with a univariate model using a LIBS setup under atmospheric pressure.

All these authors used distinct standards and experimental setups for calibration. In any case, they preferred univariate models to quantify lithium, strontium, rubidium, and barium. As a result, using the univariate method to calibrate these elements with ChemCam seems reasonable.

2.4.2. Previous ChemCam Trace Element Calibrations

Fabre et al. [2014] calibrated lithium and strontium by using the CCCT's synthetized glasses doped with these elements onboard Curiosity. *Ollila et al*. [2014] calibrated Li, Sr, Rb, and Ba with additional geological standards by using the ChemCam flight model (FM) in Martian conditions (P_{CO2} ~ 9 mbar).

Fabre et al. [2014] quantified Li by using the Li I 670.7 nm line for univariate calibration. *Ollila et al*. [2014] used the ChemCam flight model (FM) under Martian conditions (P_{CO2} ~ 9 mbar). They used the Li I 670.7 nm line to build a univariate calibration using geological standards. They also tested partial least square (PLS) multivariate analysis on the full spectra, on the spectral range (e.g., VNIR spectrometer range only), and on a reduced wavelength range focusing on 33 channels over the Li I 670 nm and Li I 813 nm peaks. This latter and the univariate calibration provided very similar results, but they preferred the univariate model since fewer negative values were predicted. Their root-mean-square error of prediction (RMSEP) is 40 ppm.

Fabre et al. [2014] quantified Sr by using the Sr II 421.7 nm line for univariate calibration. They calculated a RMSE of 154 ppm. *Ollila et al*. [2014] built a univariate calibration by using the Sr II 421.7 nm line on various geological standards and only igneous samples. They also tested PLS on the full spectra, on the spectral range, and on a reduced wavelength range focusing on 27 channels over Sr II 407.89 nm, Sr II 421.67 nm, and Sr I 460.86 nm lines. They observed greater accuracy by using only igneous standards. This latter PLS and the univariate models are very similar, but they chose to quantify data from the first 100 sols of Gale using PLS since univariate estimates are slightly higher across the concentration range. Their RMSEPs were respectively 160 and 170 ppm.

Cousin et al. [2011] detected several Rb lines on various geological materials with a ChemCam mast unit and Ocean Optics spectrometers, and with samples under a simulated Martian atmosphere. *Ollila et al*. [2014] used the Rb I 780.2 nm for a univariate calibration by using 53 reference standards. They also tested PLS on the full spectrum, on the spectral range (VNIR spectrometer range), and on reduced wavelengths focusing on 10 channels over Rb I 303.28/303.30 nm and Rb I 780.2 nm lines. This latter PLS model and the univariate were both used for the first 100 sols quantification since they are very similar. Their RMSEPs were respectively 30 and 50 ppm.

Table 2. Summary Table of Li, Sr, Rb, and Ba Quantifications of ChemCam Data

	Input	Peak Fitting					Calibration Equation	Validity	RMSE (ppm)	LOD (ppm)
		Peak (nm)	Function	Baseline	Range (nm)	Deconvolution (nm)				
Li	Clean Calibrated Spectra[a]	670.97	Lorentz	Parabolic	669.9–674.0	Si: 670.12 Ca: 671.85	$y = 4.04\ E6\ x^2 + 34060x$	Area $< 1.8\ E-3$	5	5
Sr		421.67			421.4–422.3	Ca: 422.055	$y = 7.99\ E9\ x^2 + 17.16\ E5\ x$	Area $< 4.0\ E-4$	150	87
Rb		780.24			779.3–781.0	None Ti: 454.6	$y = 2.83\ E7\ x^2 + 27.77\ E4\ x$	Area $< 1.2\ E-3$ Area $< 1.2\ E-3$	34	26
Ba		455.55			454.4–456.2	455.09 455.68 Ti/Si: 455.35	$y = 3.74\ E9\ x^2 + 18.81\ E5\ x$	$SiO_2 < 70$ wt %	334	120

[a]Clean Calibrated Spectra (CCS) are processed spectra as described in *Wiens et al*. [2013].

Ollila et al. [2014] used the Ba II 455.53 nm line for univariate calibration by using 55 various geological standards. They also tested PLS on the full spectra, on the individual spectrometer ranges (violet and VNIR spectrometer ranges), and on reduced wavelength ranges of 30 channels over each of the following emission lines: Ba II 455.53 nm, Ba II 493.55 nm, Ba II 614.34 nm, Ba I 650.06 nm, and Ba I 728.23 nm. This latter PLS model tends to predict slightly higher values than the univariate, and there is considerable scatter between the abundances, but there is a fairly good correlation between the two models. Both were used for barium quantification for samples in Gale crater. RMSEP values are respectively 670 and 640 ppm.

Fabre et al. [2014] used eight standards for calibration including four glasses and four synthetic ceramics, corresponding to the CCCTs [*Wiens et al*., 2012]. Even if calibration using the onboard standards prevents any bias between Martian and laboratory environments, the low number of samples, their nature, and texture are not diversified enough to match with Gale materials. In addition, lithium contents in the ceramics are similar, providing only five distinct concentrations in only a narrow compositional range. As a result, using a laboratory database with more numerous and various standards with a larger compositional range than *Ollila et al*. [2014] and *Fabre et al*. [2014] studies is useful for calibration.

In conclusion, *Ollila et al*. [2014] tested both univariate and multivariate analysis. They showed that the PLS method is valid and comparable to univariate results when focused on reduced wavelength ranges around the selected lines from samples under a simulated Martian atmosphere and using the ChemCam flight model. Most authors prefer to calibrate Li, Sr, Rb, and Ba by using univariate models rather than PLS. As a result, using univariate calibrations seems reasonable.

3. New Calibration Curves

Table 2 summarizes the final parameters used for calibrations and for Martian quantifications for each element. Table 3 compares *Ollila et al*. [2014] calibrations and predictions with this study.

3.1. Lithium

3.1.1. Lithium Calibration

As discussed in *Ollila et al*. [2014], an unresolved doublet at 610.52/610.52 nm, a second unresolved Li doublet at 670.96/670.98 nm, and a third unresolved Li doublet at 812.85/812.87 nm can be studied for quantification. Here we prefer to use the doublet at 671 nm since it is still present even at the lowest concentration in the data set [*Ollila et al*., 2014]. We normalize each spectrum to the VNIR range. This selected peak is shown in Figure 2a. However, a Si line at 670.12 nm and a Ca line at 671.85 nm can interfere with lithium peaks. Thus, these peaks are carefully deconvoluted to be able to separate the different elements.

In the new database a few standards contain very high Li concentrations: GUWGNA with 2276 ppm and five other samples having between 100 and 1000 ppm of lithium: SRM97A (510 ppm), SRM98A (325 ppm), UNSZK (278.74 ppm), SGR1 (147 ppm), and GBW07311 (131 ppm). All others contain concentrations lower than 72 ppm as presented in Figure 1. It is important to notice that 90% of this new database display Li contents below this value. Since 99.9% of the Martian lithium data have peak areas corresponding to under the 72 ppm from the database, we prefer to focus on these low values for all following lithium models. This "restricted database" contains 95 standards.

Table 3. Comparison of Li, Sr, Rb, and Ba Calibrations of ChemCam Data[a]

		Ollila et al. [2014]	This study
Lithium	Number of standards	32	88
	Calibration model	Univariate	Univariate
	RMSE (ppm)	36	5
	Comments	Standards < 510 ppm Some negative values	Standards < 72 ppm No negative values
Strontium	Number of standards	59	170
	Calibration model	PLS[b] and univariate	Univariate
	RMSE (ppm)	160	150
	Comments	No sedimentary standard	No outlier standard (UNSAK)
Rubidium	Number of standards	53	106
	Calibration model	PLS[b]	Univariate
	RMSE (ppm)	33	34
	Comments	Standards < 257 ppm	Standards < 413 ppm
Barium	Number of standards	55	255
	Calibration model	PLS[b] and univariate	Univariate
	RMSE (ppm)	640 - 670[c]	334
	Comments	No Si-rich standards Some negative values	No Si-rich standards No negative values

[a]Comparison between *Ollila et al.* [2014] and this study calibrations and ChemCam predictions. Predictions are generally in agreement between the two calibrations, but with improvements in accuracy in most cases.
[b]PLS used here is called PL3 in *Ollila et al.* [2014] and reduced the wavelengths to several channels around the selected peaks.
[c]The 640 ppm is the RMSE of PLS3, and 670 ppm is the RMSE of the univariate model.

Four calibration curves have been obtained for lithium (Figure 3). Two of them, "restricted-lin" and "restricted-pol," use all standards from the new database (-lin for linear and -pol for polynomial). The two others, "low_std-lin" and "low_std-pol," consider only standards having low-peak-area standard deviations, e.g., <0.2 times the mean. Samples that are heterogeneous at the LIBS spot scale are thus disregarded.

Considering this database, a linear calibration curve (restricted-lin: gray line in Figure 3a) passing through 0 fits all the data quite well. The resulting RMSE is good, 5.8 ppm, but the highest Li contents (>53 ppm) are less constrained and are quite underestimated (Figure 3a). Thus, applying a second-order polynomial law (restricted-pol: dashed black line in Figure 3a) that may reflect potential self-absorption in the plasma better predicts low and high values (Figure 3a), with a RMSE of 5.7 ppm.

If we now consider this database only including standards displaying the lowest standard deviations (88 standards), characteristic of quite homogeneous standards, a linear function ("restricted-low_std-lin") fits the data quite well but may also underestimate high values (gray line in Figure 3b). A second-order polynomial law ("restricted-low_std-pol") better constrains the data (dashed black line in Figure 3b). The two RMSEs are nearly identical, with 5.4 ppm and 5.3 ppm, respectively.

These accuracies are relatively good, and the polynomial functions give a better fit to the considered range of abundances. In LIBS calibration this polynomial form is classically observed for light elements with low first ionization potentials and is usually due to self-absorption [*Fabre et al.*, 2002; *Sweetapple and Tassios*, 2015].

Looking at the residuals of polynomial models in comparison with linear models, we can observe in Figures 4a and 4b that they are very similar. Low abundances are better constrained by the polynomial calibrations. For higher values, polynomial and linear models both give similar results.

We applied the calibrations described above to the CCCTs analyzed both in the laboratory and on Mars, even though they are not the most relevant standards for Li. We averaged these lithium predictions for each CCCT and calculated their standard deviation. Due to their high Li contents, the ceramics and macusanite samples are out of the range of our database and thus poorly constrained (the actual values are 7433 ppm and 3528 ppm, respectively, compared to the predicted values being 1100 ppm and 650 ppm, respectively). The norite, picrite, and shergottite glass standards (CCCTs) contain very low amounts of lithium (see Table 1). As shown in Figure 5, they are poorly constrained, with an accurary, RMSEP (root-mean-square

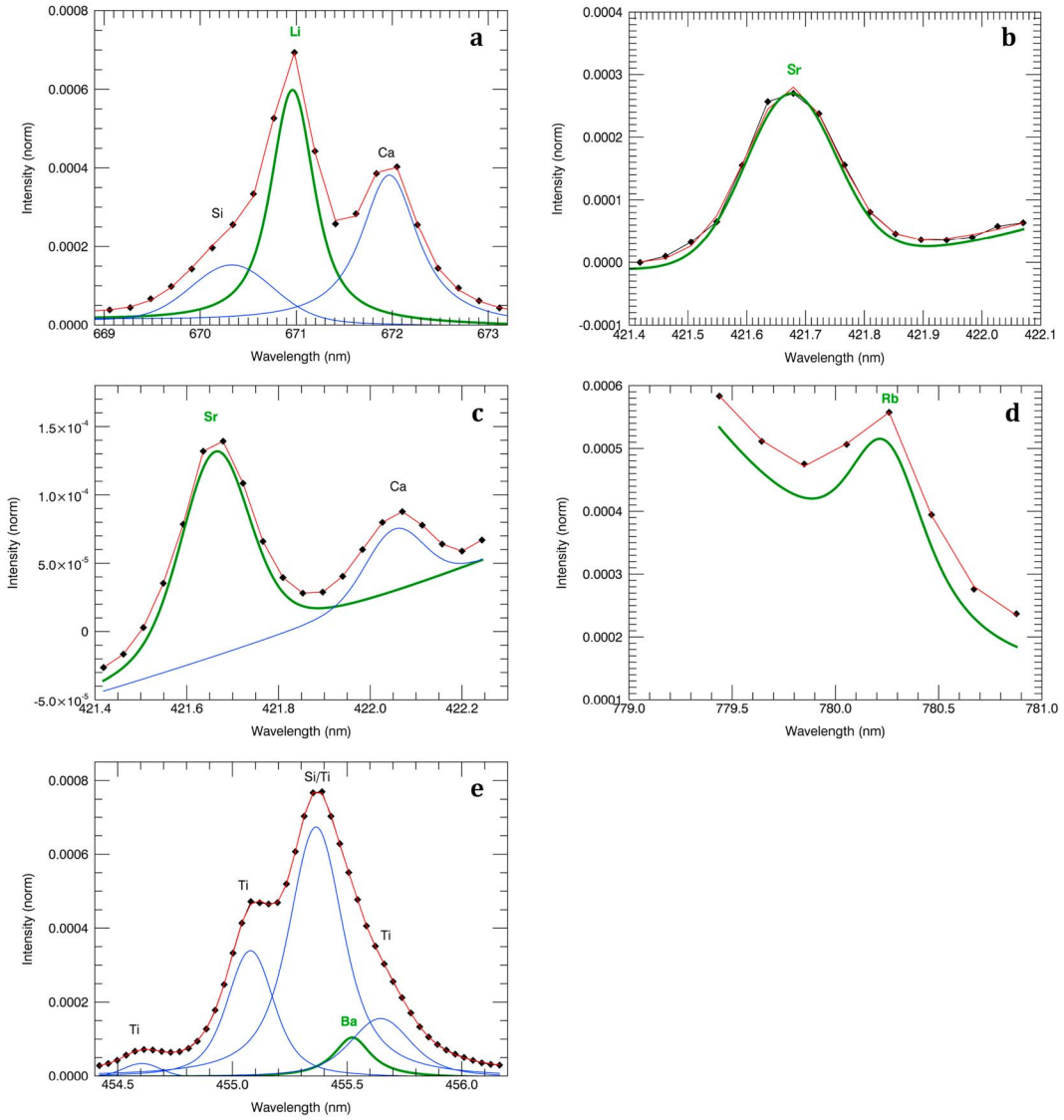

Figure 2. Peak fitting of (a) Li 671 nm line for Coronation target, (b) Sr 421.7 nm line fitted solely, and (c) Sr 421.7 nm line fitted with Ca 422.01 nm line for BCR2 laboratory standard. Peak fitting of (d) Rb 780 nm line and (e) Ba 455.5 nm line for coronation. The green curves are the fit of the studied trace elemental lines, the blue curves are the deconvolutions of other elements, and the red curves are the sum of the deconvolutions.

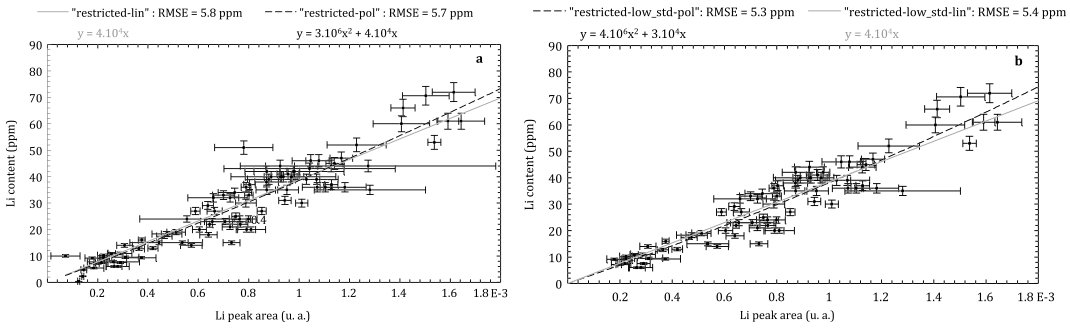

Figure 3. Li calibration curve considering (a) the whole restricted database and (b) standards with low standard deviations; i.e., for each standard, averaged areas with a standard deviation higher than 25% are removed. The area unit is presented in arbitrary unit (a. u.).

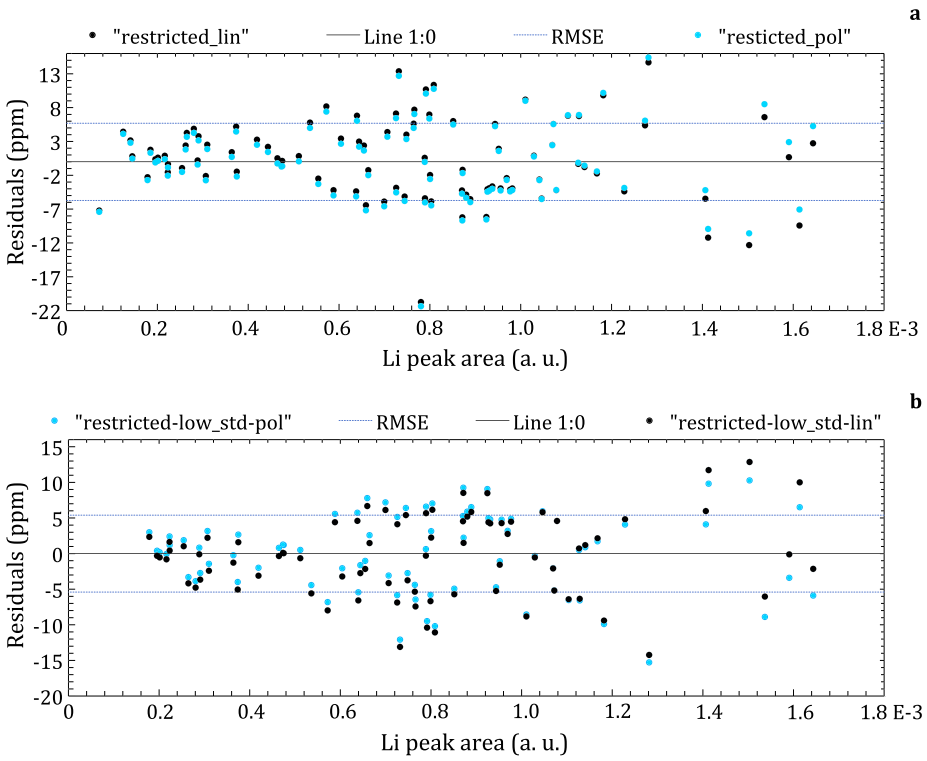

Figure 4. Residuals of (a) "restricted_lin" predictions (black dots) and "restricted_pol" (blue dots) and (b) restricted-low_std-lin (black dots) and restricted-low_std-pol (blue dots). The black dashed line is the 0:1 line. The blue dashed line is ±RMSE models (5.3 and 5.4 ppm). The area unit is presented in arbitrary unit (a. u.).

error of prediction) of ~12 ppm except picrite. This has been also observed in *Ollila et al*. [2014]. On the other hand, laboratory CCCTs replicate are well predicted. This discrepancy may be explained by either physical processes occurring on Mars that would affect Li areas of only norite and shergottite or else an issue with the Li measurements in the flight model CCCTs. Since Earth and Mars units were made from the same material at the same time, no independent analyses were performed on the actual flight units.

In general, when considering the other standards, the accuracies of these models appear to be relatively good. As we prefer to use the regression with the best accuracy, the second-order polynomial law on the restricted database with low standard deviation (restricted-low_std-pol) will be used for future in situ Li estimates (Figure 3b). The limit of detection (LOD) is low, at 5 ppm. Table 2 summarizes the details of this calibration.

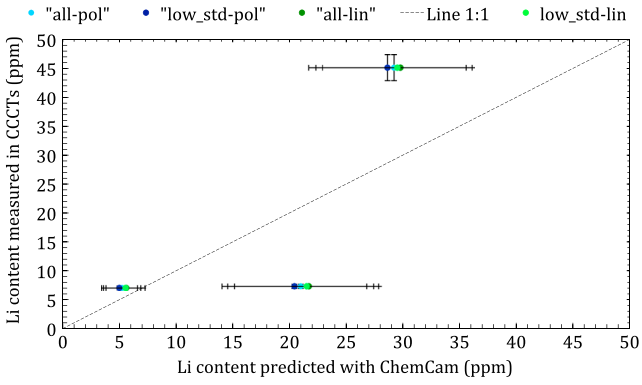

Figure 5. Li concentration measured in ChemCam onboard calibration targets (CCCTs) with LA-ICP-MS versus averaged Li concentration predicted with our calibrations. The *x* axis error bars are the standard deviations of the lithium predictions, and the *y* axis error bars are the standard deviations of the lithium composition analyzed by LA-ICP-MS.

3.1.2. Comparison of Li Estimates With Previous Study

As shown in Table 3, *Ollila et al*. [2014] considered the entire former database including four values higher than 100 ppm (up to 510 ppm; SRM97A, SRM98A, UNSZK, and SGR1), while their Martian abundance estimates covering targets observed during the first 100 sols were always lower than 100 ppm. The Li RMSE value determined by the *Ollila et al*. [2014] univariate model was 7 times higher than that obtained

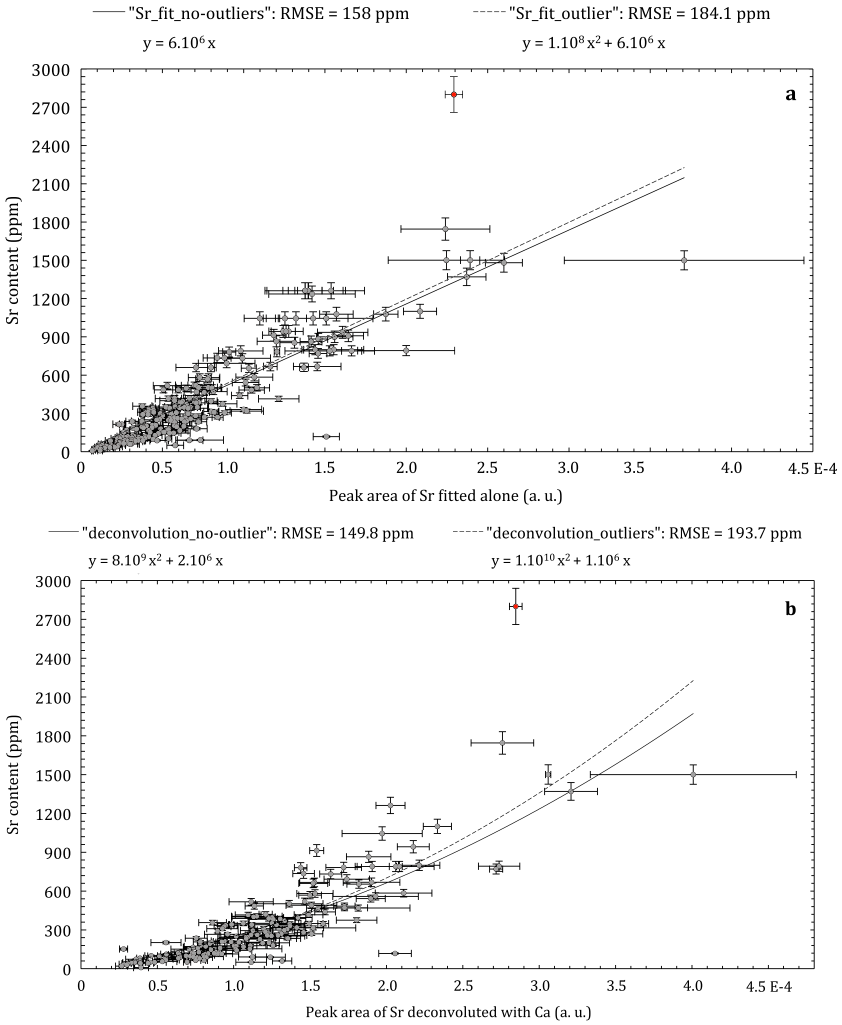

Figure 6. Calibration curves using Sr peak area (a) without fitting the Ca line and (b) deconvoluting the Ca line. The red dot is the outlier UNSAK. The black filled curve is the best fit quadratic obtained considering the database without outliers, while the dashed curve includes outliers. The area unit is presented in arbitrary unit (a. u.).

here. Moreover, their lithium predictions seem to be underestimated, especially for those higher than 25 ppm. Our regression curve, passing through the origin, avoids the negative predictions for the lowest Li peak areas that occurred in the *Ollila et al*. [2014] estimates.

3.2. Strontium

3.2.1. Strontium Calibration

Several Sr lines can be studied, as described in *Ollila et al*. [2014]: Sr II 407.89 nm, Sr II 421.67 nm, and Sr I 460.86 nm. As Fe lines strongly overlap the 407.89 nm and the 460.86 nm lines, using the 421.67 nm peak for univariate calibration is preferable. This line is bounded by a Ca II line at 422.01 nm. We normalize each spectrum to the VIO range. In order to optimize our fitting, different calibration curves have been carefully tested, two using Sr areas from Sr fitting solely and two using Sr areas from deconvolution of Ca and Sr peaks (see Figures 2b and 2c).

As we did with the lithium calibration, here we attempt a calibration always considering standards with Sr areas more than 5 times their standard deviations, either with or without outlier standards that plot far from the calibration curve: only UNSAK (Sr = 2800 ppm) is considered as an outlier. At least, more than 170 standards were selected. One hundred thirty-six standards are lower than 500 ppm (among them, 35 standards have Sr $<$ 100 ppm), 26 are between 500 and 1000 ppm, and 8 standards have Sr contents greater than 1000 ppm, with up to 2800 ppm in UNSAK as presented in Figure 1.

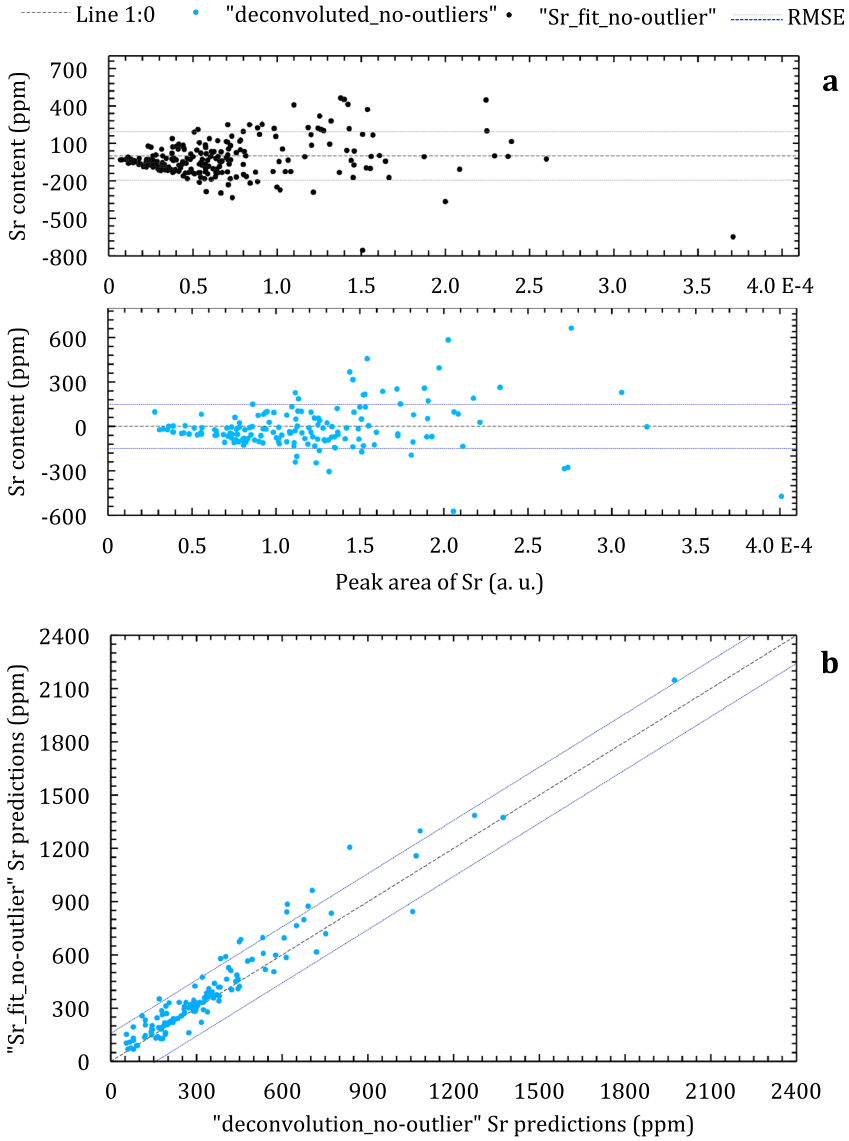

Figure 7. (a) Residuals of Sr_fit_no-outlier predictions (black dots) and "deconvoluted_no-outliers" (blue dots). The black dashed line is the 0:1 line. The dashed gray line is ±root-mean-square error (RMSE) of the Sr_fit_no-outlier model, while the dark blue dashed line is ±RMSE of the deconvoluted_no-outliers model. (b) Strontium predictions of the laboratory database standards using Sr_fit_no-outlier model versus deconvolution_no-outlier model. The dashed gray line is the 1:1 line; the light blue dots are the laboratory predictions, and the dashed dark blue lines are the RMSE of Sr_fit_no-outlier model (±158 ppm). The area unit is presented in arbitrary unit (a. u.).

3.2.1.1. Simple Sr Fits

Using areas from Sr fit on a reduced range, "Sr_fit_no-outlier" calibration excludes UNSAK that is too far from the calibration curve (Figure 6a). The Sr-richest sample is then MO7 with 1745 ppm of strontium. A linear function is the best fit, and the RMSE is 158 ppm. Using the whole database (i.e., including UNSAK), "Sr_fit_outlier," we can define a calibration curve by using a second-order polynomial regression. The RMSE is significantly higher, 184 ppm, but this regression predicts high values better than Sr_fit_no-outlier as shown in Figure 6a. We can observe that models using the restricted database, with or without outliers, tend to overestimate values lower than 200 ppm (Figure 6a).

3.2.1.2. Sr and Ca Peak Deconvolution

Here Ca and Sr peaks have been deconvolved, and we exclude the outlier sample UNSAK ("deconvolution_no-outliers"). The best fit is a second-order polynomial function. The RMSE of 150 ppm is significantly lower than the previous attempt (see Figure 6b, solid line).

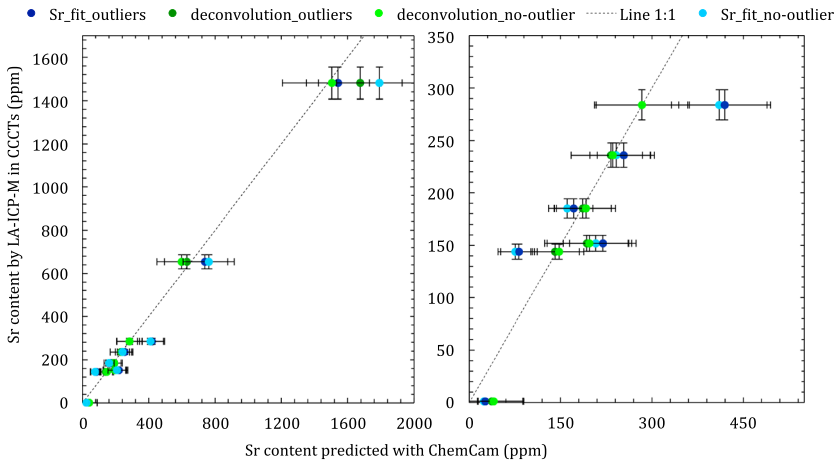

Figure 8. CCCT Sr content measured with LA-ICP-MS versus the averaged Sr predictions using the various calibrations. The graph on the right side is a zoom of Sr < 350 ppm. The *x* axis error bars are the standard deviations of the strontium predictions, and the *y* axis error bars are the standard deviations of the strontium compositions analyzed by LA-ICP-MS.

Using the entire database ("deconvolution_outliers"), including UNSAK, we obtain a second-order polynomial regression with a relatively high RMSE, at 194 ppm, but this calibration overestimates less than deconvolution_no-outliers for values lower than 300 ppm and also predicts the higher Sr abundances better (see Figure 6b, dashed line). Therefore, fitting the data by using peak deconvolution enables us to build calibration curves that are more accurate for the low values.

As presented in Figure 7a, residuals of "deconvolution_no-outlier" and Sr_fit_no-outlier calibrations increase with higher peak areas. The first model predicts the compositions better than "Sr_fit_no-outliers." Moreover, comparing Sr predictions of laboratory standards by using the deconvolution_no-outlier and Sr_fit_no-outlier models presented in Figure 7b shows that their values are very similar except some that are outside of the RMSE (158 ppm; dark blue dashed lines) due to relatively higher predictions calculated by Sr_fit_no-outlier regression.

Concerning the CCCTs, they contain a large range of strontium concentration from 1.3 ppm to 1252 ppm, covering almost the whole range of the laboratory database. These four regressions have been applied to the CCCTs onboard Curiosity. We averaged these values for each CCCT, and the predictions obtained by using the simple Sr fits yield a shift of the predicted values, especially for the silicate glasses, as they are slightly overestimated (see dark and light blue circles in Figure 8). This shows that calibrations using areas from deconvolution of Ca and Sr emission lines improve the model and are closer to actual Sr values. However, the Sr abundance in the picrite sample is overestimated by deconvolution_outliers, while deconvolution_no-outlier predicts the strontium abundance better. Thus, it is preferable to fit both the Sr and Ca lines, and database outliers should be removed (deconvolution_no-outlier). With this curve, as written in Table 2, the limit of detection is 87 ppm.

3.2.2. Comparison With Previous Study

Ollila et al. [2014] used a simple fit to the strontium line (no Ca line deconvolution) and considered a more restricted database (<59 standards). As described in Table 3, they decided to remove samples such as MHC1356 and MHC2319 which displayed high Fe and low Sr, and sedimentary samples (carbonates, sulfates, and Al-clays). This selection optimized the model in terms of agreement with the predominant geological materials encountered in Gale crater up to that point [*Ollila et al.*, 2014]. However, since then, many sulfates and clays have been analyzed [*McLennan et al.*, 2014; *Nachon et al.*, 2014]. Thus, including high-Fe standards in our models became essential in terms of representing the entire suite of sample types encountered along the mission. The RMSE obtained with this new calibration is almost the same as *Ollila et al.* [2014] (see Table 3). Moreover, considering Ollila's univariate calibration model, standards with Sr < 300 ppm are also overestimated, while their multivariate model yields higher abundances than their univariate model for low concentrations <500 ppm.

3.3. Rubidium

3.3.1. Rubidium Calibration

Three resolved Rb peaks exist in ChemCam spectra: Rb I 303.3 nm, Rb I 780.24 nm, and Rb I 794.3 nm. However, the first line is observed in only few spectra such as GUWGNA, and Rb I 794.3 nm is significantly

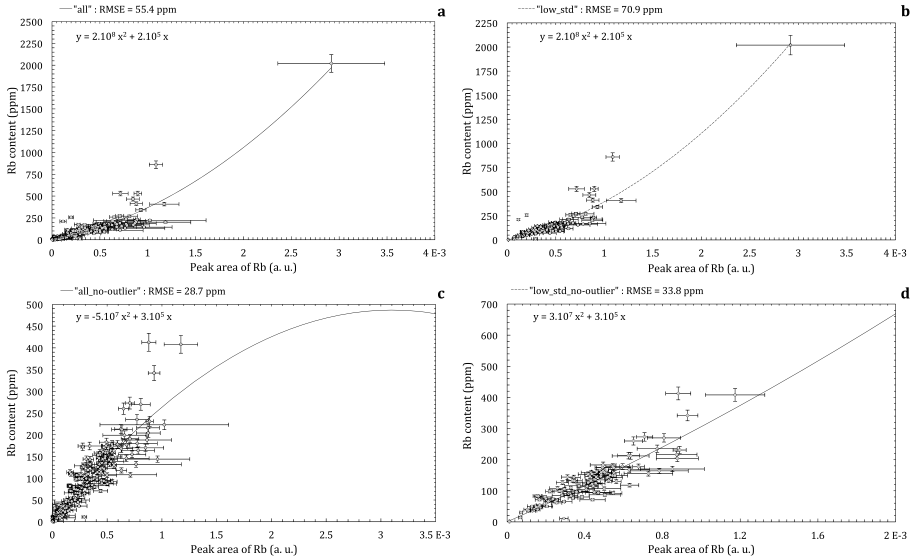

Figure 9. Calibration curves of Rb: (a) all, (b) low_std, (c) all_no-outlier, and (d) low_std_no-outlier. The area unit is presented in arbitrary unit (a. u.).

overlapped by an O line [*Ollila et al*., 2014]. Thus, the 780.24 nm peak was selected. We normalize each spectrum to the VNIR range. This line is located on the edge of an unresolved trio of O I peaks at 777 nm. If we deconvolute Rb from these three lines, then it is not possible with our algorithms to correctly fit the emission of Rb, which is much smaller than the oxygen lines. Thus, we decided to only integrate the Rb peak on a restricted range from 779.3 to 781 nm (Figure 2c).

Four calibration curves were considered, based on the averaged emission areas: two models use the mean areas of all peaks that are at least 5 times higher than the standard deviations, and either included outlier samples ("low_std") or did not ("low_std-no_outliers"). Two other models are based on the whole standard database including outliers ("all") or not ("all-no_outliers").

Figure 1 presents the Rb abundance distribution in the database. Eighty-one standards contain between 100 and 400 ppm of Rb, and 176 are $<$100 ppm, i.e., 30.7% and 66.7% of the database, respectively. Five standards contain between 600 and 400 ppm. The highest Rb content is 2020 ppm in GUWGNA, followed by UNSZK with 860 ppm. Thus, out of a total of 264 samples, most of the standards have $<$400 ppm.

For the calibration curves using the entire data set (all and low_std), we obtain second-order polynomial regressions for the LIBS emission areas versus Rb compositions (Figures 9a and 9b). For the all calibration, the RMSE is quite good, at 55.4 ppm, but values at $<$150 ppm seem to be underestimated (Figure 9a).

Low-sigma selection restricted the database to 113 standards but still included high Rb samples (2020 ppm, 860 ppm, and the five with 400–600 ppm of Rb). The selection also included 53.1% of the samples in the 100–400 ppm range and 40.7% with Rb contents under 100 ppm. The RMSE is similar to the previous model, at 70.9 ppm (see Figure 9b). We notice that using only the standards that appear to be more homogeneous (with low sigma), the low Rb samples ($<$200 ppm) are better constrained than the all calibration curve.

Seven outliers were removed from the initial database due to their high abundances and strong deviations from the fitted curve: GUWGNA (2020 ppm) with higher Rb than the rest of the database, UNSZK (860 ppm), JSC1387 and JSC1388 (529.2 ppm), GBWO7103 (466 ppm), JR1 (257 ppm), and JSC1374 (210.41 ppm). Even if the peak areas of these standards fit the curve well we would still consider these samples as outliers, as they are poorly constrained for at least one of the other elements studied in this paper. Therefore, the remaining highest Rb content considered in this restricted database is JSC1425 with 412.7 ppm. Fitting Martian data, only 22 locations corresponding to 0.66% of the data, have a peak area higher than the maximal area in the laboratory database. Based on this, we conclude that removing these outliers is reasonable. We just need to note that these 22 targets may be poorly estimated in terms of rubidium content. The two following models, "all-no_outlier" and "low_std_no-outlier," exclude these outliers.

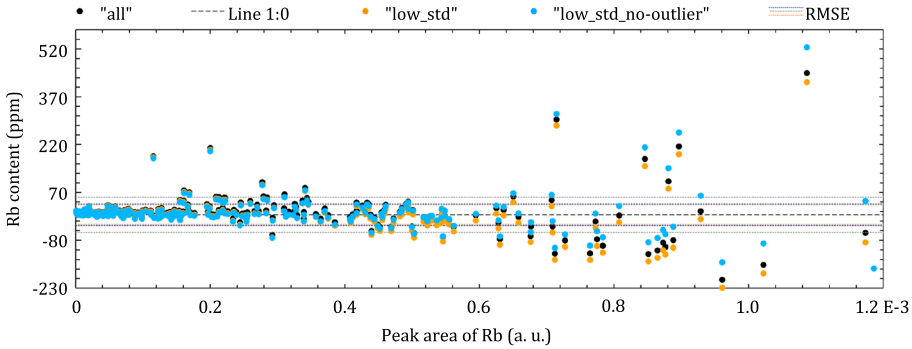

Figure 10. Residuals of all (black dots), low_std (orange dots) and low_std_no-outlier (blue dots) models. The dashed gray lines are the RMSE of the first calibration, the dashed orange lines are the RMSE of the second calibration, and the dashed dark blue lines are the RMSE of the latter calibration. The black dashed line is the 1:0 line. The area unit is presented in arbitrary unit (a. u.).

Considering this database (all-no_outlier), a second-order polynomial regression fit yields better agreement to all of this set of data. The calculated RMSE of 28.7 ppm is better than those obtained with all standards (all) (see Figure 9c). We notice that the lowest values are better constrained than by the previous models, in contrast to high Rb abundances, which appear to be underestimated. The major issue with this model is that the polynomial function turns over, with the maximum being located around an area of 3.10^{-3} as shown in Figure 9c. This calibration curve should therefore not be used for lines intensities above $\sim 1.5 \cdot 10^{-3}$.

If we use only standards with average abundances that are 5 times lower than the standard deviations (low_std_no-outlier), a second-order polynomial law is preferred over a linear one. This final RMSE reaches 33.8 ppm (see Figure 9d). However, the expected values at $<$100 ppm are not well constrained in comparison with those of the "all_no-outlier" model. The lack of standards at these low values may explain this scatter. Yet standards with high Rb contents are better constrained than previously in that the polynomial function is continuously increasing.

The residuals of all versus low_std_no-outlier and low_std versus low_std_no-outlier are plotted in Figure 10. Low values are well predicted in all models. Yet low_std predictions from areas of 4.10^{-4} to 6.10^{-4} are poorly constrained in comparison with low_std_no-outlier. High-abundance data are not well estimated, but the model excluding the outliers seems to result in better predicted values.

Thus, the low and high values are better constrained when using only standards with low standard deviations and removing outliers from the database: e.g., the best model is the low_std_no-outlier model (see Table 2 for more information). Therefore, this regression is used to predict Martian data, giving a limit of detection of 26 ppm.

3.3.2. Comparison With Previous Study

As described in Table 3, *Ollila et al*. [2014] preferred using PLS, reducing the wavelength range to only 10 channels around Rb I 303.28 nm and Rb I 780.24 nm, since this model appeared more accurate than the univariate model. Their RMSE is similar to ours (Table 3).

Moreover, *Ollila et al*. [2014] calibrations focused on laboratory data with lower Rb than our study, while actual targets encountered in Gale present values are higher than this limit (see Table 3). As a result, their two models of calibration would need to be more often extrapolated than ours for some Mars targets. The univariate calibration used by *Ollila et al*. [2014] tends to overestimate predicted laboratory data up to ~300 ppm in comparison with our regression. As they observed that this model underestimates samples with abundances $<$100 ppm in comparison with PLS, this multivariate algorithm overestimates the laboratory data even more. Thus, it appears that our new model fits standards better than previous models.

3.4. Barium

3.4.1. Barium Calibration

Five Ba lines can be detected: Ba II 455.53 nm, Ba II 493.55 nm, Ba II 614.34 nm, Ba I 650.06 nm, and Ba I 728.23 nm. However, in contrast to the study of *Essington et al*. [2009], the most sensitive line for barium using the LANL test bed under Martian conditions is Ba II 455.5 nm, which can be observed down to

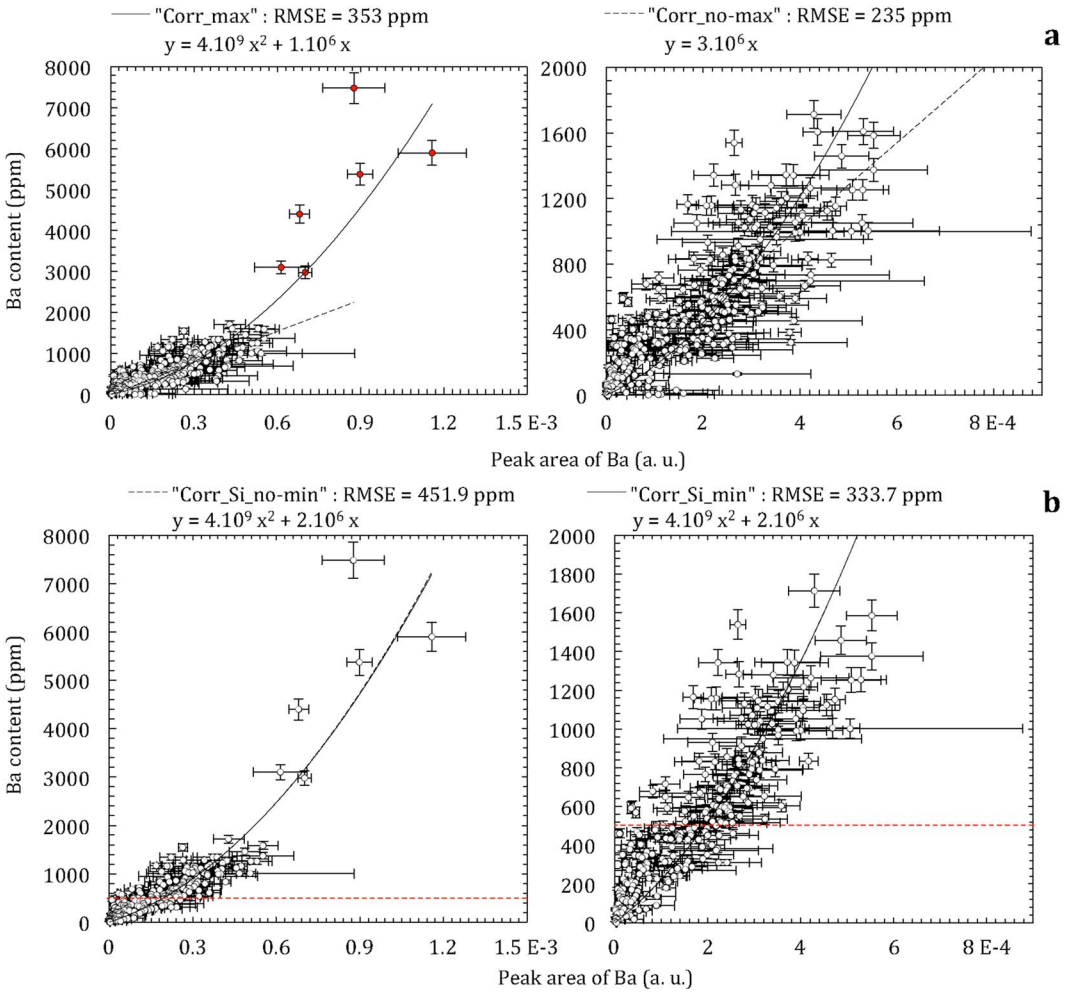

Figure 11. Calibration curves of barium considering (a) the entire corrected database and (b) the corrected database without Si-rich outliers. The red dots in Figures 11a and 11c are the samples higher than 2000 ppm not considered in Corr_no-max nor "No-Corr_no-max" calibrations. The dashed red line in Figure 11b separates samples with Ba lower than 500 ppm that are not considered in Corr_Si_no-min model. Graphs on the right side are zooms of Ba < 2000 ppm. The area unit is presented in arbitrary unit (a. u.).

100 ppm [*Ollila et al*., 2014]. We normalize each spectrum to the VIO range. This emission line is surrounded by five peaks: Ti III 454.597 nm, Ti II 455.23 nm, Ti I 455.34 nm, Si III 455.40 nm, and Ti I 455.785 nm. This Ba line is present as a bump on the descending part of a combined Ti-Si peak in typical spectra of silicate rocks. All of these emission lines are deconvolved (see Figure 2e), but the close proximity of the multiple interfering peaks complicates the fitting as already described in *Ollila et al*. [2014].

For Ba calibration, we consider the entire new database with 307 standards. Its distribution is presented in Figure 1. Eighty-nine standards are in the 500–1000 ppm range, and 167 are <500 ppm. Forty-five are between 1000 and 2000 ppm, while six contain more than 2000 ppm of Ba. IGS29 and SARM16 samples have 5900 ppm and 5374 ppm, respectively, and the highest Ba is observed for standard MO7 with 7480 ppm. Here we present four calibrations: two of them are based on this whole database including high Ba contents "Corr_max" and removing them "Corr_no-max," and two others are calculated without Si-rich standards ($SiO_2 > 70$ wt %) including data lower than 500 ppm "Corr_Si_min" and removing them "Corr_Si_no-min."

Concerning the whole laboratory database, a first calibration curve called Corr_max was constructed with a second-order polynomial function passing through zero. As observed in Figure 11a (the solid line), standards are widespread below 2000 ppm, while above this value, they are poorly predicted. The RMSE is 353.4 ppm. Considering only Ba abundances at <2000 ppm, a linear function Corr_no-max fits the standards quite well.

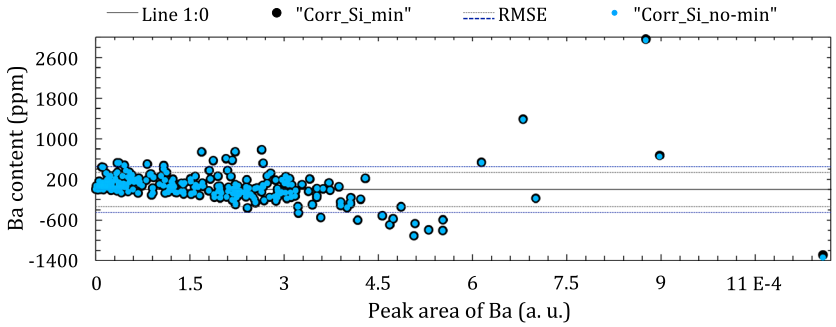

Figure 12. Residuals of Corr_Si_no-min (blue dots) and Corr_Si_min (black dots) models. The dashed dark blue lines are the RMSE of the first calibration while the dashed gray lines are the RMSE of the latter calibration. The black dashed line is the 1 by 0 line. The area unit is presented in arbitrary unit (a. u.).

Figure 11a shows that this calibration applied to laboratory data predicts lower values than Corr_max estimations above 700 ppm. There is a scattering of values in this range (see the dashed line in Figure 11a). Even so, the accuracy is better, with a RMSE of 235 ppm. This large scattering of values may be due to interferences between the barium emission line and silica and/or titanium emission lines, which are nearly on top of each other. Removing samples with high Ti content ($TiO_2 > 2.6$ wt %) does not change the calibration curve significantly, whereas excluding Si-rich standards ($SiO_2 > 70$ wt %) results in less scattered regressions (see Figure 11b). The Si emission line clearly modifies the Ba predictions at high Si abundances.

Considering this restricted database, a second-order polynomial regression Corr_Si_min is deduced with a RMSE that is higher than Corr_no-max but lower than Corr_max (333.7 ppm). Intermediate values between 600 and 1600 ppm are better constrained with Corr_Si_min than the two previous models (Figures 11a and 11b). However, values at $<$500 ppm are badly constrained for every model. This is true even if Ba lines are well fitted. Corr_Si_no-min is a model where these values are removed (i.e., data below the dashed red line in Figure 11b are not used for this model). A second-order polynomial regression is the best fit with a RMSE of 451.9 ppm (see the gray dashed line in Figure 11b). Yet this model and Corr_Si_min are close. Figure 12 shows their residuals with the real Ba compositions of the silica-restricted laboratory database. Again, both are very similar. We notice that the RMSE is higher in Corr_Si_no-min since only higher-abundance standards are considered. Therefore, since both calibrations predict almost the same values, we decided to focus on the regression by using a more complete Si-restricted database, i.e., Corr_Si_min.

Excluding high silica samples tends to improve predictions of Ba concentrations. Indeed, Ba integrated emissions are often overestimated due to the Si line influence, and thus, the slope of the calibration curves increases when this spurious influence is removed. In each case, applying these regressions to CCCTs analyzed on Mars with ChemCam and averaging these barium concentrations for each CCCT shows relatively good predictions for low values, i.e., norite and ceramic standards. However, high Ba contents in picrite and shergottite are underestimated (see Figure 13a). Calculating the RMSEPs on CCCTs, the most accurate calibration would be Corr_Si_min with 179 ppm against 234 and 224 ppm for Corr_max and Corr_no-max, respectively. Indeed, predicted Ba contents in picrite and shergottite are closer to their actual compositions, but they are still underestimated, with 805 and 705 ppm, respectively, versus 1283 and 1158 ppm actual abundances. However, looking at their barium contents predicted from laboratory LIBS observations, Ba in picrite and shergottite is also underestimated, while their Si and Ti contents are similar to other standards. This may be due to a coupling issue. Therefore, even if the accuracy is worse than Corr_no-max, including samples with high Ba content and excluding outliers with high Si give a calibration that increases predicted values at high concentrations. Thus, CCCTs are better constrained, but still underestimated for picrite and shergottite. Since Corr_Si_min predicts the low and high Ba abundances in CCCTs better, this model is preferable, with a LOD of 120 ppm (see Table 2).

3.4.2. Comparison With Previous Study

As described in Table 3, *Ollila et al.* [2014] PLS method focused on a restricted number of channels covering the Ba peaks. Since their univariate model displayed relatively similar results, both models were used to yield abundances of Mars targets. Looking at Ollila's predictions of the CCCT Ba abundances, both models dramatically underestimated barium concentrations in picrite and shergottite silicate glasses (predictions

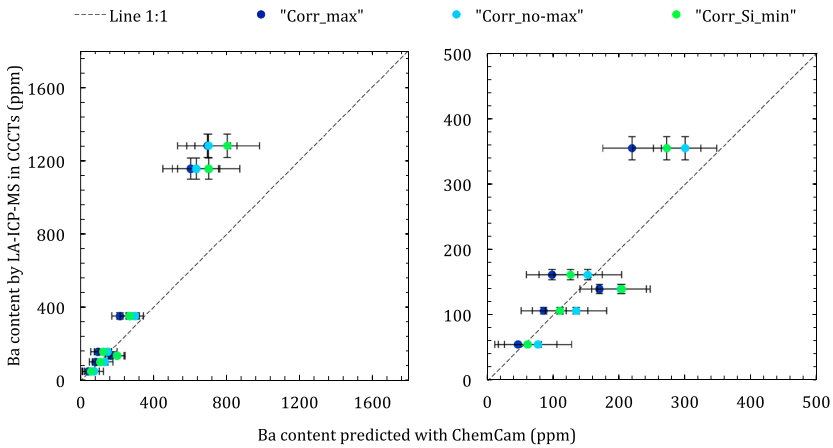

Figure 13. Comparison of Ba content measured in CCCTs with LA-ICP-MS and the averaged predictions using the various models. The graph on the right side is a zoom of Ba < 500 ppm. The *x* axis error bars are the standard deviations of the barium predictions, and the *y* axis error bars are the standard deviations of the barium compositions analyzed by LA-ICP-MS.

of ~790 and 780 ppm, respectively, against real values of 1283 and 1158, respectively), but norite and ceramics were quite well predicted. In this paper, our univariate predictions undertaken on onboard CCCTs are improved. Moreover, considering Ollila's calibration curve [*Ollila et al*., 2014], we notice an overestimation for low values (<1000 ppm).

Ollila et al. [2014] PLS and univariate models both predict some negative values, while we use calibration regressions passing through the origin to avoid this discrepancy. We also note larger RMSEs than ours (see Table 3).

3.5. Summary of Li, Sr, Rb, and Ba Calibration Models

In conclusion, we have quantified Li, Sr, Rb, and Ba abundances by using univariate models based on second-order polynomial regressions passing through the origin. All these calibrations are based on standards containing trace amounts that cover the ranges of Martian peak areas well. Lithium, strontium, and rubidium models exclude outliers. Indeed, models with outliers are less accurate and give poorer CCCT predictions. Li and Rb models focus on standards with low standard deviations, and Sr calibration is better constrained when fitting both Sr and Ca line in spectra. Barium is calibrated with standards containing $SiO_2 < 70$ wt % since the strong Si line interferes too much with the Ba line.

Applying these regressions to Martian data enable us to predict their concentration. The method is summarized in Table 2. As shown in Table 3, these models predict similar values as *Ollila et al*. [2014] except a few lower abundances predicted with our regression for barium, but remaining within the RMSEPs (e.g., Akaitcho 7: 670 ppm using their univariate calibration, 570 ppm using PLS and 409 ppm with our model).

4. Trace Element Enriched Targets: Geological Implications

Using the calibrations of Li, Sr, Rb, and Ba described above, we apply the quantification models to ChemCam data corresponding to the first 1000 sols. We can note that the accuracy of these values is obtained from the previously calculated RMSE shown in Table 2. These quantifications enable the study of trace element variations along Curiosity's traverse and their possible mineralogical associations or geological processes that may explain their abundances. As a reminder, each ChemCam target is sampled by several LIBS observation points, each point being analyzed by 30–50 shots. LIBS spot size varies from 350 μm to 550 μm depending on the distance to the target [*Maurice et al*., 2012]. As a result, larger minerals can be analyzed as nearly pure phases, while smaller minerals would be sampled along with the matrix and/or other phases. Numerous LIBS points contain more elevated amounts of Li, Sr, Rb, and Ba than most ChemCam data and are considered as outliers (all data higher than 3 times the interquartile ranges). The averaged trace element composition for each target shows that outliers correspond to materials with averages of Li > 38 ppm, Sr > 280 ppm, Rb > 207 ppm, and Ba > 459 ppm. These enrichments are associated with specific minerals within igneous and sedimentary rocks and are the results of magmatic phenomena referring to the partitioning of

Table 4. Summary Table for Each Point and Target Containing Elevated Amounts of Trace Elements

	Target	Nature of the Target	Minor Enrichment	Classification	Rationale
Magmatic targets	Becraft	Float rocks	Ba, Rb	Trachyte	K substitutions within whitish alkali feldspar
	Chakonipeau		Ba		
	Sledgers				
	MeetingHouse_2				
	Wilkinson			Quartz-diorite	
Sedimentary targets	Mc Sherry no. 5	Coarse-grained sandstone	Li	K-Mg-Sandstone	Association with alkali feldspar
	Carrara	Fine-grained sandstone	Sr	K-Sandstone	Ca/K substitutions within clay mineral
	Perdido				
	Frome_Rock nos. 3, 5, and 6	Pebbles	Rb, Li (no. 5)	K-Mg-Pebbles	Association with Mg-mica
	Egan no. 4	Pebbly sandstone	Rb	Conglomerate	
	Kalumburo no. 3	Pebble	Rb, Sr, Ba	Feldspathic Pebble	K substitutions within sanidine

preferential trace elements during partial melting and fractional crystallization, and/or secondary processes such as erosion [*Heier and Billings*, 1970; *Wedepohl*, 1978; *Ure and Berrow*, 1982; *Lyons and Welch*, 1997; *Deer et al*., 2001]. The following sections focus on these targets by identifying which mineral(s) or other phase(s) host such trace elements and investigating processes that may have led to their enrichments. Table 4 summarizes these associations for each point and target subsequently described. Some of these points are poorly constrained since their peak area is higher than the maximum area used for calibration (see Table 2), and are indicated by one or two asterisks in Table S1 in the supporting information.

4.1. Trace Enrichments in Igneous Rocks

Lithium, strontium, rubidium, and barium enrichments are mainly related to their compatibility during magmatic processes. Here we discuss these enrichments and their implications.

The highest whole rock Rb content (230 ppm) is observed in Becraft, analyzed on sol 421. This rock is apparently a vesicular float rock located in the Cooperstown area consisting of millimeter and micrometer white crystals within a grayish matrix interpreted as a trachyte [*Sautter et al*., 2015; *Cousin et al*., 2017] (Figure 14). Note that the LIBS spot size is often smaller than these crystals, enabling almost-pure mineral analysis, like in point 5. Becraft's averaged composition reveals particularly high SiO_2 and K_2O reaching 76.8 and 4.2 wt %, respectively, in point 3 where barium is the most elevated, with 1000 ppm (see Table S1). Al_2O_3 and Na_2O are also moderate to high in comparison with most ChemCam data (see Table S1). These elevated values, along with appearance of the target point as a light-toned mineral, suggest the occurrence of Na-K-rich feldspar, confirmed by a Cross, Iddings, Pirsson, and Washington (CIPW) norm suggesting approximately 40% plagioclase and 25% orthoclase. Rubidium and barium may be related to these potassic minerals. This is in agreement with higher K_2O contents when Rb is elevated. In addition, positive trends between Ba and orthoclase abundances calculated from the CIPW norm, support their occurrence within these feldspars. Moreover, point 5 is the highest in rubidium, with 443 ppm (where the abundance is relatively uncertain due to a lack of standards in this abundance range). Looking at the RMI mosaics taken before and after LIBS shots

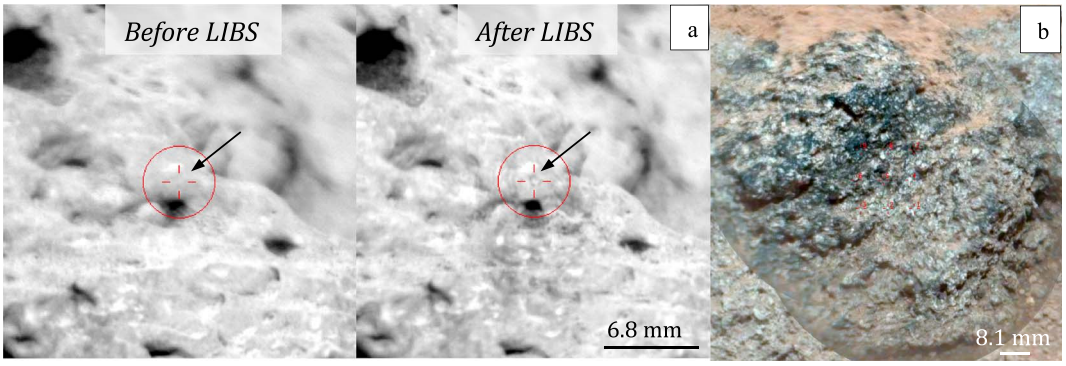

Figure 14. RMI image of (a) Becraft point 5 before and after LIBS shot. The black arrows are the location of the laser shot and show the appearance of a whitish grain after LIBS. (b) RMI image merged with a colored Mastcam image of Wilkinson.

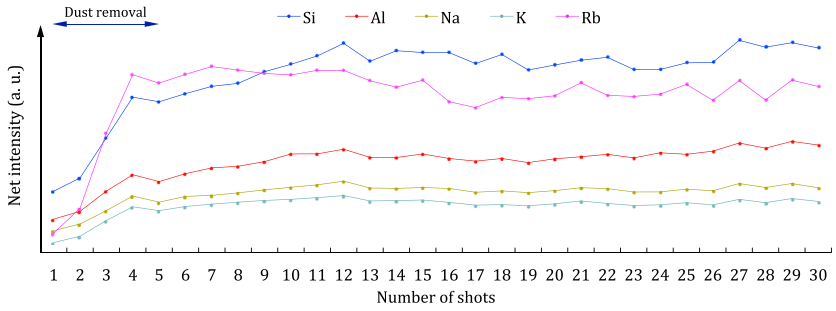

Figure 15. Elemental peak intensity trends with depth in point 5 of Becraft.

(Figure 14a), the grayish material has been removed, and a white crystal measuring around 470 μm, i.e., slightly larger than the LIBS spot size, appears at the surface. This mineral is interpreted as an alkali feldspar regarding elevated SiO_2, Al_2O_3, Na_2O, and K_2O contents. Since FeO and MgO contents are depleted but not equal to zero (4.19 wt % and 1.49 wt %, respectively), it is likely that the feldspar sampled by ChemCam is slightly contaminated by the grayish matrix. Depth profiles in Figure 15 reveal increases of Rb, Al, K, Si, and Na intensities for the first five shots, while remaining shots display quite constant intensities. This suggests that immediately after dust removal, the laser probed an alkali-alumina-rich silicate, i.e., a light-toned alkali feldspar as inferred by the RMI mosaic. Therefore, we suggest that rubidium is associated with alkali feldspars in this trachyte. This is in agreement with an enrichment of barium often seen in terrestrial K-bearing minerals [*Deer et al*., 2001]. As observed on Earth in *Deer et al*. [2001], elevated amounts of Rb and Ba in this target along with high alkali, silica, and aluminum contents relative to most ChemCam data reinforce the idea of a high degree of differentiation in the source magmatic system or a low degree melting of the Martian mantle in agreement with *Sautter et al*. [2016].

The highest Ba targets detected by ChemCam are encountered in Chakonipau, Sledgers, and MeetingHouse_2 float rocks, located in the Hummocky Plains and observed on sols 338, 381, and 653, respectively. These rocks have been classified as cryptocrystalline trachytes [*Sautter et al*., 2015; *Cousin et al*., 2017]. Note that the barium concentration in Sledgers no. 4 may be poorly estimated, but remains elevated. The LIBS spot being larger than the grain size in these fine-grained felsic targets, each LIBS point sampled a mixture between the matrix and minerals (RMI available on NASA's Planetary Data System).

All three targets are in average Ba-rich, SiO_2-rich (>60 wt %), and alkali-rich ($Na_2O + K_2O$ >7 wt %), see Table S1). As described earlier, the Ba emission line of choice is spectrally close to an interfering Si line, but in this case an asymmetric Si peak displaying a large bump on its right side validates the occurrence of a significant Ba peak. Al_2O_3 is elevated (>15 wt %), while CaO is low (mainly <4 wt %). Lithium, strontium, and rubidium compositions are moderate to low in comparison with most of the ChemCam. A CIPW norm calculation performed on ChemCam major element compositions reveals high amounts of felsic materials such as plagioclase: 45% in Chakonipau, 28.5% in Sledgers, and 45.5% in MeetingHouse_2, and orthoclase: >14% in all of these samples. This suggests that Ba is associated with these potassic minerals.

Besides point 2 that contains the lowest Ba concentration, Chakonipau barium contents display a strong positive correlation with aluminum and a slight positive trend with an orthoclase component calculated from the CIPW norm. This supports Ba association within these minerals. In addition to elevated Ba concentrations, Sledgers contains three points, nos. 1, 5, and 8, which also have high Sr contents. Interestingly, Sr, Ba, Al_2O_3, and Na_2O are strongly positively correlated, and so are Ba and K_2O contents. This also suggests the occurrence of these elements within alkali phases, specifically their correlations with plagioclase and orthoclase abundances calculated from CIPW. As a result, Sr and Ba would be mainly hosted within these two types of minerals mixed within the matrix. MeetingHouse_2 points display positive correlations between Rb and Ba, and Sr and Ba. This suggests their occurrence in the same phase. In addition, Ba and K_2O contents display positive trends with the orthoclase component from the CIPW calculations (except point 1 containing lower Ba). Hence, barium would be mostly contained within these potassic minerals.

Wilkinson (observed sol 365) is another rock encountered in the Hummocky plains and enriched in barium, with an average of 495 ppm. Note that the barium content in point 7 may be poorly estimated due to a lack of

standards in this abundance range. Unlike the previous target, it is a coarse-grained rock with granoblastic texture showing micrometer-size white crystals interpreted as feldspars and classified as a quartz-diorite/granodiorite by *Cousin et al*. [2017] (Figure 14b). Indeed, the high averages of SiO_2 (62.3 wt %) and alkali contents (>7 wt %) are associated with high alumina content (19.8 wt %). The CIPW norm suggests 68% plagioclase and 21% orthoclase. The Li content is low, with moderate Sr and Rb concentrations (35 and 132 ppm, respectively). We can observe that Rb, Ba, SiO_2, Al_2O_3, Na_2O, and K_2O concentrations are positively correlated, suggesting their occurrence within an alkali-alumina-rich silicate phase. This is supported by strong positive trends of Rb and Ba with orthoclase abundances and slighter correlations with plagioclase abundances calculated from the CIPW norm. Therefore, barium and rubidium are likely mainly hosted within these light-toned felsic minerals.

In conclusion, alkali feldspars are the main source of Sr, Rb, and Ba in these evolved igneous rocks. This has been observed on Earth within a wide range of alkali-rich rocks. For instance, in unaltered alkali basalts from the Mid-Atlantic ridge at 43°N, the bulk barium and strontium concentrations are more elevated in rocks containing the highest bulk potassium content and the highest orthoclase abundances from the CIPW calculations (Sr = 1240 ppm, Ba = 500 ppm, K_2O = 1.59 wt %, and Or = 9.4 % in rocks 3–10) [*Shibata et al*., 1979]. Indeed, these elements tend to easily replace potassium in these crystals and behave incompatibly: they were likely concentrated along with K, Al, and Si during partial melting or late-stage differentiation of a magmatic system [*Deer et al*., 2001].

4.2. Trace Enrichments in Sedimentary Rocks

Lithium, strontium, rubidium, and barium enrichments in sedimentary rocks are usually related to source materials, sedimentary deposition, and/or erosion. Below we discuss the observed enrichments of these elements in Gale sedimentary targets. All but two of them are located in the Kimberley region, which is characterized by potassic sandstones. The other two were found in a nearby soil-filled depression informally called Hidden Valley (sols 705–720).

Most of the Li-rich targets are analyzed in rocks containing high alkali contents: (1) Rocknest_3_2, a vuggy layered outcrop analyzed at sol 83 at Yellowknife Bay, with point 8 containing up to 102 ppm; (2) Frome Rocks, millimeter-size pebbles and soil with micrometer-size white minerals smaller than the LIBS spot size within a darker matrix in a few pebbles, located on sol 584, with point 5 reaching 119 ppm; and (3) McSherrys point 5, a millimeter-size white grain that appeared homogeneous in the RMI image, in a sandstone encountered in the Liga member in the Eastern Kimberley on sol 594, with 77 ppm of lithium. Note that Li contents in Frome_Rocks no. 5 and McSherry no. 5 may be poorly estimated due to the lack of standards in this abundance range. Rocknest_3_2 lithium enrichment has been already discussed by *Ollila et al*. [2014] and is thought to be associated with an Al-rich silicate that has a detrital origin. We will thus focus on the other targets.

Frome_Rocks consists of three points, nos. 3, 5, and 6, located on pebbles. According to the RMI, LIBS points have sampled the whitish minerals and the darker matrix. They are high in magnesium, potassium, and rubidium and moderate to high in lithium (see Table S1). Point 5 has the highest lithium content measured by ChemCam, with 119 ppm, and displays the highest potassium (K_2O = 5.6 wt %), magnesium (MgO = 18.3 wt %), and rubidium (Rb = 586 ppm) contents in this target. Note that Rb content may be poorly estimated. Shot by shot analysis in point 5 shows an increase of Li with depth and strong correlations with Mg, K, Al, and Si, with similar slopes and slight positive trends with Na and Rb (Figure 16a). Ca is inversely correlated with Li. Moreover, a strong CaF signature is observed [*Forni et al*., 2015]. ChemCam's detection limit for fluorine is about 0.2 wt %, and this element has been already found in Gale crater as Ca-depleted Al-rich silicates and fluoroapatites and/or fluorites [*Forni et al*., 2015]. This minimal amount of F and positive correlations between Mg, K, Al, Si, Rb, and Li in point 5 support the occurrence of a Li-F-bearing Mg-K-Al-rich silicate like mica [*Foster*, 1960; *Ure and Berrow*, 1982]. In addition, a few clay minerals like illite can also include F, Li, and Rb within their structure [*Millot*, 2013]. As a result, one of these phases may be the host of lithium: the capacity of Li to substitute for Mg and Al can explain the positive correlations observed between those elements [*Kogel*, 2006]. Mica is not observed by CheMin in the Windjana drill sample, located at Kimberley [*Treiman et al*., 2016]. This is completely consistent with our results, as ChemCam showed no fluorine within the Windjana drill hole itself even though F was observed in nearby targets. We must conclude that the presence of mica is variable in these sediments. Weathering of micas produces illite and then smectite

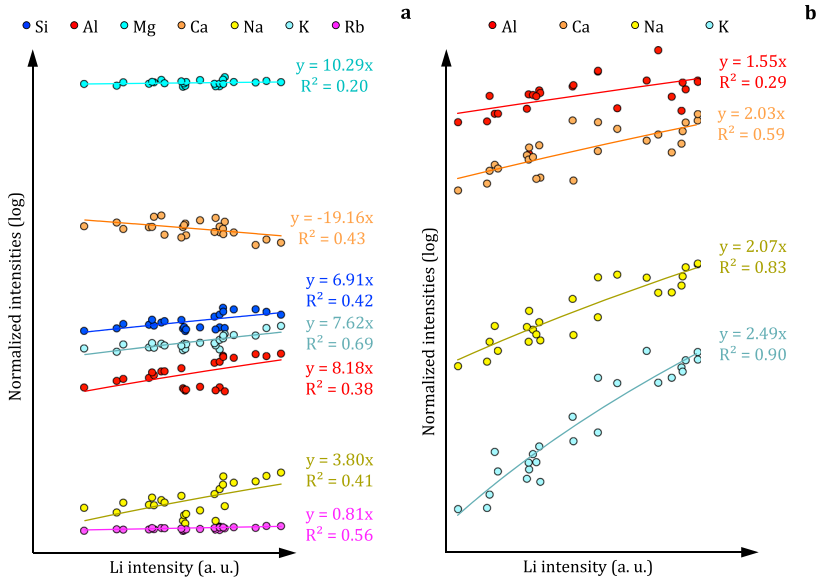

Figure 16. Li I 671 nm peak intensity variations versus elemental intensity trends without dust contribution in (a) Frome Rock point 5 and in (b) Mc Sherrys point 5. Correlation coefficients and slopes of each lineary trend are indicated.

[*Deer et al*., 2001], which are identified by CheMin. In addition, Martian meteorite magmatic inclusions contain some of this phase [*Johnson et al*., 1991; *Brearley*, 1998]. Therefore, the presence of micas as a source of lithium seems very reasonable [*Forni et al*., 2015]. The occurrence of Li within a F-bearing Mg-alkali-rich clay like illite, as observed in several locations on Earth, is also conceivable [*Millot*, 2013]. An alternative is the incorporation of lithium within a Mg-rich amorphous phase, as the amorphous component inferred by CheMin and APXS in the Windjana sample (MgO ~ 21.6 ± 9.6 wt %) [*Treiman et al*., 2016].

The homogeneous light grain McSherrys (point 5) displays the highest lithium content in this target with 77 ppm (Li in points 1–4 and 6–10 are <11 ppm). It is likely LIBS sampled a single phase or a mix of micrometer-size minerals smaller than the RMI resolution and a whitish matrix. In contrast to other locations, this point is particularly enriched in Al_2O_3, with 28.2 wt %, and in K_2O, with 2.8 wt %, and is MgO-poor, with 0.9 wt %. Shot by shot analysis reveals various trends in Li intensity with depth as shown in Figure 17: the Li signal increases during the first five shots corresponding to the dust removal [*Meslin et al*., 2013] and is constant until shot no. 14, where Li intensity starts decreasing. This suggests that LIBS analyzed a specific grain enriched in lithium, located at the surface between shot 6 and 13. Li is strongly correlated with K, Ca, Na, and Al, as inferred by similar high slopes in Figure 16b. Thus, a feldspar grain could have been sampled by LIBS from shot nos. 6 to 13 and would be a potential source of lithium. This pebble grain displaying a distinct composition in comparison with the other McSherry points supports an inherited chemistry from its source, and thus a detrital origin in agreement with *Le Deit et al*. [2016].

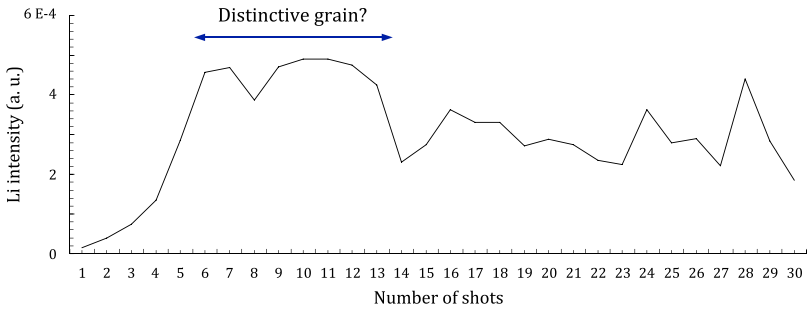

Figure 17. Li 671 nm peak intensity trends with depth in point 5 of Mc Sherrys.

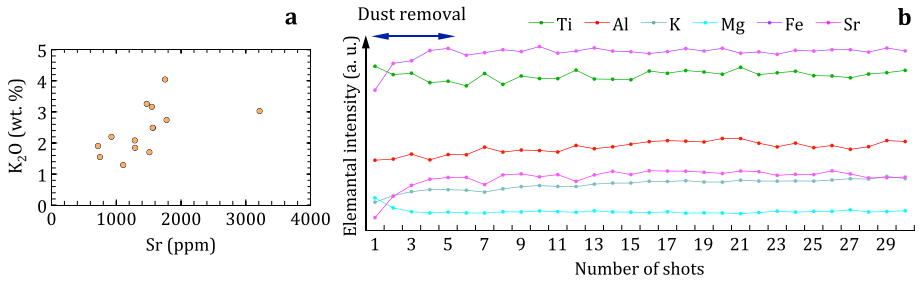

Figure 18. (a) Strontium content versus potassium in Perdido and (b) elemental peak intensity trends with depth in point 7 of Perdido.

In conclusion, lithium is mainly associated with K-bearing phases in alkali grains. At Kimberley, *Le Deit et al*. [2016] suggested that potassic minerals have primarily a detrital origin, with at least two major sources, one being K-rich igneous rocks and the other low-alkali basaltic rocks providing mafic minerals [*Treiman et al*., 2016]. The feldspar in McSherry point 5 would be the source of lithium and is the most elevated in K_2O content in this target. It could thus come from potassic igneous rocks. In Frome_Rock point 5, the occurrence of potassic micas or other phyllosilicates as lithium-fluorine-rubidium hosts may have a similar origin. As well documented on Earth by *Lyons and Welch* [1997], lithium that is mobile at low pH may have originated within these minerals due to strong K-Li (-F) affinity. This type of acidic environment has been already described by *Nachon et al*. [2016] for the formation of dendritic aggregates and the occurrence of ferric sulfates at Pahrump Hills. Another hypothesis is that Li may have been liberated by the weathering of primary igneous minerals and incorporated in potassic minerals like phyllosilicates and feldspars prior to sedimentation.

Most of the Sr-rich targets are encountered in rocks containing high alkali contents: (1) Soledad_Pass, a Fe-K-rich filled fracture observed on sol 794, with 2695 ppm with a standard deviation σ of 8211 ppm (due to a unique point displaying a very high Sr content, described below); (2) in Link, a felsic conglomerate with millimeter-size white, grayish, and dark grains observed on sol 27, with 1424 ppm ($\sigma = 460$ ppm); (3) in Carrara, a K-rich float rock with hundreds to few micrometer-size white grains within a darker matrix containing 1690 ppm ($\sigma = 475$ ppm) (points 1, 2, and 3 only, the others are located in the soil); and (4) in Perdido on sol 725 with very similar texture, with 740 ppm ($\sigma = 430$ ppm) of strontium. Note that strontium concentrations in Carrara no. 3 and Perdido no. 13 may be poorly estimated due to the lack of standards in this abundance range. These elevated Sr values are measured in all points for each target. Therefore, these enrichments are not local and may suggest alteration processes. As strontium enrichments in Link and in Soledad_Pass have been already discussed in *Ollila et al*. [2014] and *Nachon et al*. [2014] and related to strontium association with feldspar phases and Fe-K-rich phases, respectively, we will focus on the other targets.

Carrara and Perdido are particularly enriched in potassium (see Table S1). According to the RMI images, LIBS sampled generally dark-toned surfaces rather than a single whitish grain as might be indicative of a felsic clast. Their CaO contents are similar, at ~5 wt %. They have an intermediate compositions for Gale rocks, with Al_2O_3 ~10 wt % and FeO ~21 wt %. Figure 18a shows that the Perdido observation points have a strong positive correlation between Sr and K_2O contents, considering the Sr-rich locations. Strontium is thus associated with potassic phases. Depth profiles of point 7 show a constant Sr, K, Fe, and Mg composition, as presented in Figure 18b. According to the RMI image, point 7 analyzed the dark matrix, containing potassium, iron, and magnesium as well as strontium. This is consistent with higher Sr contents in the Cooperstown and Kimberley areas, where Fe-rich felsic sandstones were encountered [*Le Deit et al*., 2016]. This illustrates K-Sr substitutions and possibly also strontium adsorption on clay minerals in sandstones, as typically observed on Earth [*Short*, 1961; *Bilgin et al*., 2001].

Calcium is not generally well correlated with Sr for Gale rocks, but correlations can occur in a few targets such as in calcium sulfate veins (e.g., Deep_Spring point 9), as it has been shown for many Ca-sulfate veins displaying Sr content of 300–400 ppm [*Nachon et al*., 2014]. High strontium abundances reveal Ca/K substitutions in plagioclases such as albites and anorthites (e.g., Link [*Ollila et al*., 2014]) and/or adsorption on clay minerals. The occurrence of these latter supports aqueous alteration processes. As observed on Earth,

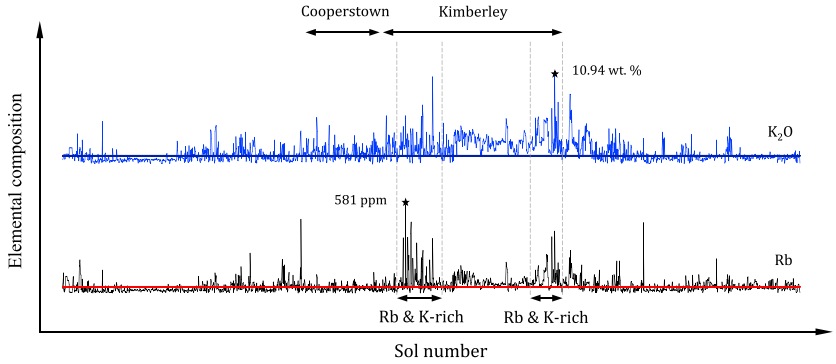

Figure 19. Rb distribution in Gale crater for ChemCam targets up to sol 1000 (black line) and Rb average (red line), and K_2O distribution in Gale crater for ChemCam targets to sol 1000 (light blue line) and its average (dark blue line). The maximum values are indicated by the black stars.

strontium could have been leached from the host rock by acidic and oxidizing fluids or simply by fluid circulation [*Short*, 1961]. Sr sorption on clays is then enhanced in more alkaline streams. These kinds of circum-neutral oxidizing environments have been already observed in Gale crater by *Lanza et al*. [2016] with the precipitation of manganese oxides in fracture fills at Kimberley.

Most of the Rb-rich targets contain elevated potassium values and are mainly concentrated at Kimberley, as shown in Figure 19: (1) Frome Rocks, discussed above in the context of Li, with 210 ppm; (2) Egan point 4, a pebbly sandstone enriched in Si, Al, Na, K, and Sr encountered in the Liga member in the northern part of Kimberley on sol 581, with 505 ppm; and (3) Kalumburo point 3, a feldspathic 2 mm size pebble cemented within a bedrock located in the Liga member in the southern Kimberley on sol 632, with 392 ppm (see Table S1) [*Le Deit et al*., 2016]. Note that their Rb contents may be poorly estimated due to the lack of standards in this abundance range.

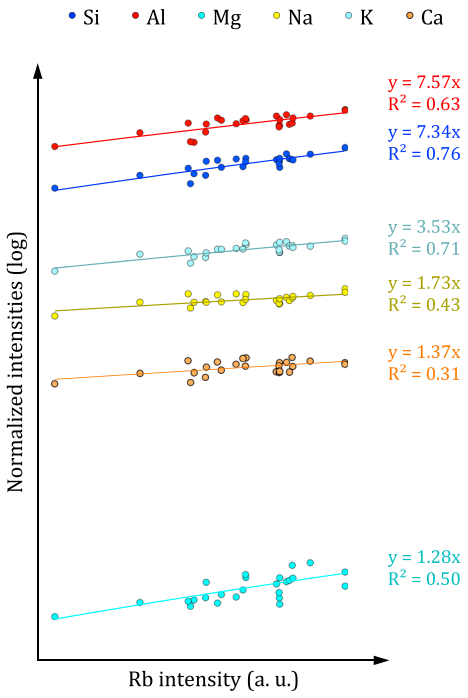

Figure 20. Rb I 780.24 nm peak intensity variations versus elemental intensity trends without dust contribution in (a) Frome Rock point 5 and (b) Egan point 4. Correlation coefficients R^2 and slopes of each lineary trend are indicated.

Point 4 probed a white pebble as part of the Egan target. According to the RMI image, the laser ablated the left part of this pebble, enabling the analysis of the grain itself. It is silica-, alumina-, and alkali-rich. Magnesium is also moderately high in this target (MgO = 6.5 wt %). Depth profiles of point 4 reveal an increase of rubidium, correlated with Si, Al, Mg, Ca, K, and Na as shown in Figure 20. A high CaF signal is also observed. This is in agreement with an association with alkali and Mg-Al-rich silicates such as clay or mica, but an apatite grain or a feldspar mixed with another phase should not be ruled out.

The highest potassium content analyzed by ChemCam is Kalumburo point 3 and displays 10.94 wt % of K_2O and a sanidine-like composition [*Le Deit et al*., 2016]. The RMI image shows that ChemCam sampled the whole whitish grain. As shown in Table S1, silica, alumina, and alkali concentrations are elevated, and iron and magnesium contents are close to zero. As a result,

the image and its composition suggest that a pure feldspar such as sanidine has been analyzed. In addition, this point is elevated in Rb, Sr, and Ba with 392, 1105, and 1178 ppm, respectively. Its depth profile reveals increasing Rb and Sr intensities with depth and positive correlations with Si, Al, Na, and K, and negative correlations with Fe and Mn. It is likely that Rb, Sr, and Ba are located in a K-bearing grain such as sanidine.

Therefore, rubidium is enriched in rocks presenting K-bearing Al-rich silicates like micas, clays, or sanidine. This suggests K-Rb substitutions as observed on Earth [*Deer et al*., 2001].

In conclusion, enrichments in trace elements in these sedimentary targets are mainly related to potassic alumina-rich silicates such as feldspars. As summarized in Table 4, most of these minerals are likely coming from K-rich igneous rocks and were transported into Gale crater as part of the sediment load and other Kimberley felsic detrital minerals [*Treiman et al*., 2016; *Le Deit et al*., 2016]. Enrichments are also due to clay minerals, which are likely authigenic, but could be detrital. Rubidium and its host phase may have originated from the same K-rich igneous rock sources [*Treiman et al*., 2016; *Le Deit et al*., 2016] since this trace element has low mobility due to its strong affinity for K-bearing phases [*Heier and Billings*, 1970; *Wedepohl*, 1978]. However, strontium and lithium are relatively mobile at low pH and could have been liberated by weathering from host minerals. In this scenario, Sr would have been adsorbed on K-phyllosilicates. Li enrichments in the potassic alumina-rich silicates can be mainly related to two processes: either the lithium originates from these minerals, or else it has been incorporated during secondary processes in these phases where the strong K-Li and/or Li-F affinities prevent the later release of these elements from these phases. Indeed, lithium is relatively immobile since fluoride compounds have low solubility especially at circum-neutral and basic pH [*Stubblefield and Bach*, 1972; *Lyons and Welch*, 1997].

5. Gale Crater Viewed by ChemCam

5.1. Bimodal Composition in Gale Crater

As described in previous studies, one of the main striking features at Gale crater so far is the discovery of silica- and alkali-rich rocks, such as feldspathic pebbles, K-rich sandstones at Kimberley, and felsic igneous rocks, together with a variety of basaltic material along Curiosity's traverse prior to arriving at the base of Mount Sharp [*Cousin et al*., 2014, 2015; *Le Deit et al*., 2016; *Sautter et al*., 2014, 2015, 2016]. As presented in *Cousin et al*. [2017], mafic rocks mainly identified as basalts and gabbros contain low silica contents ($SiO_2 < 52$ wt %). In addition, the main group of sedimentary rocks has a basaltic composition comparable to mafic igneous rocks with $SiO_2 < 52$ wt % and would originate from erosion and relithification of these basaltic materials [*Bridges et al*., 2016]. The previous section showed that Li, Sr, Rb, and Ba tend to be incorporated within potassic alumina-bearing silicates, rather than mafic minerals. As a result, in order to study their distributions in Gale's surface materials, we focus on an observed bimodal distribution of whole-rock compositions: silica-poor rocks ($SiO_2 < 52$ wt %) and silica-rich rocks ($SiO_2 > 52$ wt %).

The compositional distribution of major and trace elements is presented in the boxplots in Figure 21. Their averages are listed in Table 5. Materials with high silica reflect low iron and magnesium targets with high alkali concentrations (4.0–8.1 wt % in 75% of the data, see the boxes in Figure 21), while low silica targets are more depleted in alkali contents varying between 2.5 and 4.6 wt % in most points. Calcium is equally distributed in both groups (i.e., Ca-pyroxenes, plagioclases, and apatites and/or Ca-sulfates mixed within the host rock).

Most of the soluble incompatible trace elements, Sr, Rb, and Ba, are higher in alkali-Si-rich materials than Si-poor materials with averages of 157 ppm versus 64 ppm, 74 ppm versus 57 ppm, and 194 ppm versus 75 ppm, respectively. This is consistent with their association with alkali minerals such as alkali feldspars and K-phyllosilicates (see section 1.3). However, lithium content is quite constant in both materials. Indeed, as described in section 1.3, Li is usually associated with magnesian phases like pyroxene and Mg-micas, and with more alkali-rich minerals such as K-feldspars.

5.2. Gale Crater Composition Compared to Martian Meteorite Compositions

In this section, the previously described Gale materials are compared to Martian meteorites. The vast majority of Martian meteorites are igneous and rarely include soils; soils were therefore excluded from ChemCam data for comparison [*Rao et al*., 1999; *Barrat et al*., 2014].

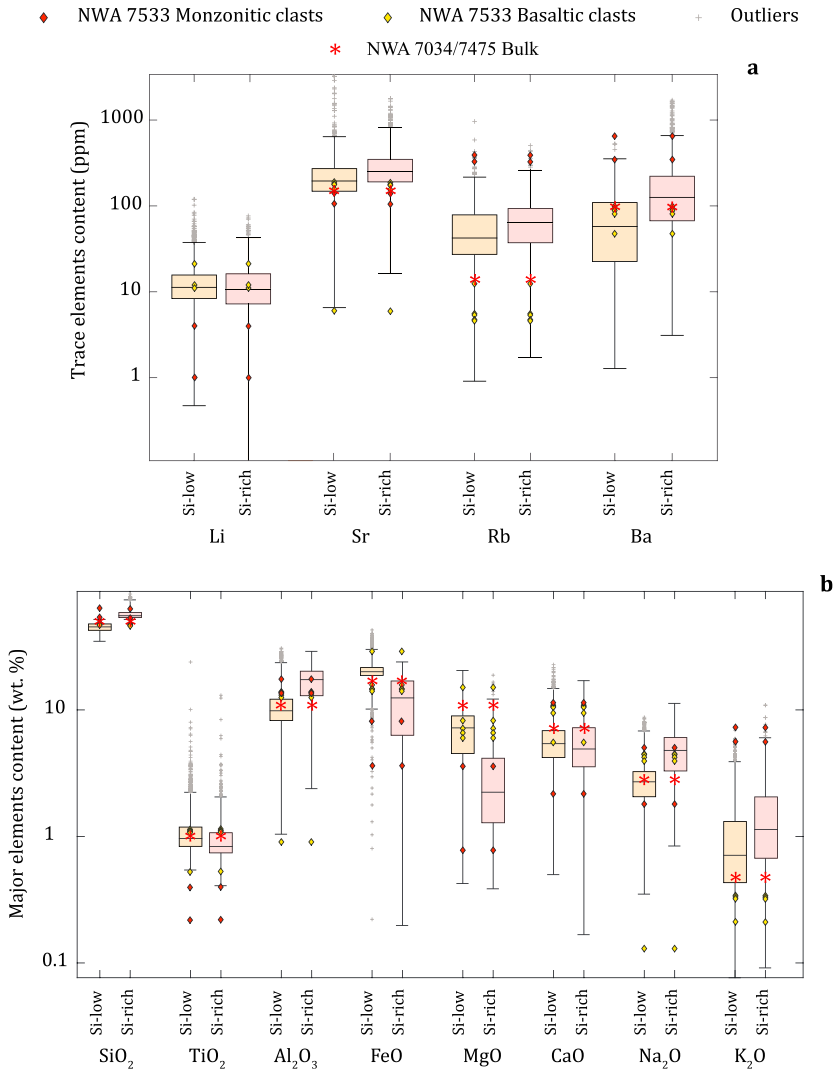

Figure 21. Box plots of (a) Li, Sr, Rb, and Ba and (b) major element abundances in silica-low (orange boxes) and silica-rich (red boxes) materials observed by ChemCam in Gale crater. The Gale median is the line in the middle of the box, the lower edge of the box is the first quartile, and the upper edge is the third quartile. The black lines on each side extend to the most extreme values except the outliers (gray crosses). The red diamonds represent the composition of the monzonitic clasts from NWA 7533, and the yellow ones show the composition of its basaltic clasts.

Around 150 Martian meteorites have been collected on Earth up to now, and most of them have been precisely analyzed [*Meyer*, 2015]. Among these Martian meteorites, ~82% are classified as shergottites, ~14% as clinopyroxenites (nakhlites), 3% as dunites (chassignites), and 1% is considered as orthopyroxenite. Most of them were found in desert surroundings such as Northern Africa and Antarctica. Their terrestrial exposure age can be important, as terrestrial contamination may occur, and the enrichment of strontium and barium contents can be considered as an evidence of such weathering. Therefore, Sr and/or Ba-rich meteorites need to be studied with caution.

Nakhlites and chassignites are coarse-grained ultramafic cumulate rocks with relatively young crystallization ages, ~1.3 Gyr, thus representing Middle Amazonian crust. Shergottites are mafic to ultramafic rocks with a wide range of Mg number (from ~15 to 75) with even younger crystallization ages, <600 Myr, thus sampling Late Amazonian crust [*Nyquist et al.*, 2001]. Therefore, the age distribution of these mafic and ultramafic SNCs is not representative of the surface age distribution observed in the Southern hemisphere (>3 Gyr) corresponding to Noachian and Hesperian ages, and in Gale crater, which most likely formed during the Early Hesperian period, 3.5–3.8 Gyr [*Tanaka et al.*, 2014]. Moreover, looking at the average compositions of these

Table 5. Average of Major Element Compositions in Oxide Weight Percent and of Trace Element Compositions in ppm in Gale for Silica-Rich and Silica-Poor ChemCam Targets Without Considering Soils, and Compositions of the Martian Meteorite NWA7533 Bulk Clasts Analyzed by *Humayun et al.* [2013][a]

	Gale ChemCam Average				NWA7533 Clast Compositions							
	Si-Poor Materials		Si-Rich Materials									
	AVG	STD	AVG	STD	Monzonitic Clast I	Monzonitic Clast II	Microbasalt Clast VI	Microbasalt Clast VI	Microbasalt Clast VI	Microbasalt Clast VI	Noritic Clast IX	Bulk[b]
SiO_2	45.2	3.6	57.3	5.2	63	53	46.7	46.5	47.6	46.6	48.2	48.3
TiO_2	1.1	0.6	1.0	0.8	0.22	0.4	1.08	1.1	1.11	1.14	0.53	1.02
Al_2O_3	10.8	3.8	16.7	4.9	17.5	13.6	12.5	13.1	13.67	13.9	0.9	10.7
FeO	20.6	4.1	11.6	6.0	3.59	8.05	15.6	14.4	13.9	14.6	28.7	16.6
MgO	7.1	3.3	3.0	2.4	0.78	3.6	8.18	7.17	6.6	6	15	10.9
CaO	5.8	2.5	5.3	2.6	2.16	11.4	9.4	10.5	10.6	10.9	5.5	7.04
Na_2O	2.8	1.1	4.8	1.7	5.01	1.81	3.92	4.22	4.4	4.5	0.13	2.8
K_2O	1.0	0.9	1.6	1.3	7.19	5.58	0.33	0.34	0.32	0.33	0.21	0.47
Total	94.1	4.9	99.8	3.7	99.5	97.4	97.7	97.3	98.2	98.0	99.2	97.8
Li	13	8	13	9	1	4	11	11	12	12	21	n.d.[c]
Sr	64	108	157	154	105	142	157	177	180	190	6	152
Rb	57	50	74	56	387	326.5	5.5	5.3	4.6	4.7	12.3	13
Ba	75	67	194	237	345	644	82	92	89	98	47	98

[a]Average composition (AVG) and standard deviation (STD) for 3701 Si-poor and 1001 Si-rich Gale points are shown.
[b]The bulk composition has been analyzed by *Wittmann et al.* [2015].
[c]n.d. for nondetermined concentration.

meteorites, most incompatible element contents (Li, Sr, Rb, Na_2O, K_2O, and Al_2O_3) are particularly low, even more depleted than low-silica ChemCam targets. This is consistent with most SNCs being mafic-ultramafic basalts and cumulates. These meteorites are neither representative of Noachian-Hesperian terrain in terms of age, nor of Gale materials in terms of chemical composition [*Nyquist et al.*, 2001; *Taylor and McLennan*, 2009].

In contrast, the recently found regolith breccia NWA 7034 [*Agee et al.*, 2013] paired with NWA 7533 [*Humayun et al.*, 2013] and NWA 7475 [*Wittmann et al.*, 2015], dated at ~4.44 Ga for the components of the breccia [*Nyquist et al.*, 2016], may be more typical example of the Noachian crust [*Wittmann et al.*, 2015; *Hewins et al.*, 2017]. While Gale crater is early Hesperian in age, the igneous basement rocks at the rim of the crater, which is the source for the clasts and sedimentary rocks in the crater, are Noachian, and so are likely to be similar in age to the Martian meteorite breccia. It is a polymict breccia consisting of a fine-grained interclast matrix with various clasts of igneous rocks including leucocratic feldspathic clasts and impact melt rocks [*Humayun et al.*, 2013]. It contains leucocratic monzonitic clasts (clast types I and II) predominantly consisting of orthoclase, Na-rich plagioclase, augite, chlorapatite, and ilmenite, along with fine-grained (20–100 μm) basalts called microbasalts and noritic clasts (clast types VI and IX) consisting of orthopyroxene, pigeonite with augite, plagioclase, minor chloroapatite, and Cr-rich magnetite. The breccia meteorite compositions are reported in Table 5 [*Humayun et al.*, 2013; *Wittmann et al.*, 2015]. The bulk composition is mafic (see Table 5) [*Agee et al.*, 2013; *Wittmann et al.*, 2015]. The boxplots in Figures 21a and 21b present their minor and major element contents divided into mafic (clast types VI and IX, yellow diamonds), felsic (clast types I and II, orange diamonds), and bulk compositions (red stars). The elemental abundances of most magnesian rocks in Gale crater are relatively similar to the bulk abundances of the breccia except for lower Rb and FeO, and higher MgO concentrations. In addition, microbasalt and noritic clast compositions are consistent with most of the low-Si Gale rocks, except for higher Rb and K. Overall, this suggests that the low-silica group from Gale has a mafic-like composition. By contrast, the high silica group contains higher SiO_2, Al_2O_3, Na_2O, K_2O, Sr, and Rb contents than the Martian breccia bulk composition, while FeO, MgO, and CaO are more depleted. Moreover, in term of silica, aluminum, magnesium, iron, sodium, and strontium most alkali-rich targets are closer in composition to monzonitic clasts. However, Gale alkaline rocks have significantly lower K_2O, Rb, and Ba concentrations, and higher Li, in comparison with these evolved meteoritic clasts. We can note that 25% of Li data (black line below the box in Figure 21a), and K, Rb, and Ba outliers (crosses in Figures 21a and 21b), overlap well with these monzonitic phases. Hence, the high silica group composition is close to a felsic-like composition. This Martian meteorite described as "a geological field conveniently aggregated

in one rock" [*Agee et al*., 2013] shares some striking similarities with Gale crater rock compositions, especially between magnesian materials as seen by ChemCam and mafic basaltic and noritic clasts. Alkali materials have a composition fairly comparable to monzonitic clasts enriched in incompatible elements, except notable lower potassium and trace element abundances. These differences between Gale rocks and the breccia compositions are likely due to distinct mineralogical assemblages: for example, no sedimentary amorphous phase was found in the meteorite [*Wittmann et al*., 2015]. In addition, we considered both sedimentary and igneous rocks in Gale while we focused on igneous clasts from the Martian meteorite: these two types of materials have distinct chemical compositions. Indeed, the abundances of major and trace elements in sedimentary rocks are affected by diverse secondary processes that are mainly dependent on host rock compositions and environmental conditions, while unaltered igneous phase compositions are driven by magmatic processes, e.g., as described in section 4.1. However, the affinity of Sr, Rb, and Ba for K-bearing minerals is strong enough to display coherent trends to the monzonitic clasts from the Martian meteorite, with more elevated amounts in alkaline materials. In conclusion, the chemical behavior of these trace elements in sedimentary and igneous rocks from Gale crater is comparable with that of the Noachian breccia.

6. Conclusion

Trace element quantification using ChemCam has been updated since *Ollila et al*. [2014] with an expanded set of standards that provides a better representation of the compositional ranges observed at Gale crater, on Mars. Univariate models were favored in this study to quantify minor elements since this straightforward method gives results as good as the multivariate calibrations sometimes used previously for these elements. The results are improved by better accuracies for Li and Ba, evidenced by the more accurate abundances provided by the calibration models for the onboard standards with known abundances. Mars target values are still consistent with the previous Mars calibrations.

ChemCam sampled materials that have a bimodal composition, being silica-poor ferro-magnesian and silica-rich alkaline, similar to the Martian breccia meteorite NWA 7533. Monzonitic clasts from this meteorite and Gale alkali rocks are both enriched in incompatible elements. However, potassium and trace element abundances are more depleted in Gale crater. The basaltic clasts from NWA 7533 and Gale magnesian rocks are both enriched in compatible elements. Li, Sr, Rb, and Ba quantified in the first 1000 sols in Gale crater on Mars are in agreement with the soluble incompatible major elements (Si, Al, Na, and K) enriched in alkali materials and depleted in more magnesian materials, similar to their composition in the meteoritic clasts. As a result, the chemical behaviors of trace elements including strontium, rubidium, and barium within the Noachian meteorite NWA 7533 and Gale crater rocks are fairly comparable, certainly due to their affinity with potassium [*Farley et al*., 2014; *Sautter et al*., 2016].

Finally, enriched lithium, strontium, rubidium, and/or barium targets have been encountered in Gale, especially in the Kimberley area where K-rich sandstones have been found, as described in *Le Deit et al*. [2016]. These enrichments are mainly related to the presence of alkali materials, particularly the K-bearing minerals groups: mica, feldspar, and K-phyllosilicate. They are mainly associated with minerals that underwent secondary processes like erosion and/or weathering (occurrence of clay minerals and detrital feldspars, for example) or that come from evolved magmatic systems or low partial melting. This provides more evidence of a complex magmatic history as described in *Stolper et al*. [2013] and *Sautter et al*. [2015, 2016], and potential surface aqueous alteration in Gale crater.

Acknowledgments
The major element compositions, LIBS spectra, and RMI images from ChemCam are listed in the tables and the supplementary table and can be found in http://pds-geosciences.wustl.edu/missions/msl/chemcam.htm. The teams supporting development, flight, and Mars operation of the *Curiosity* rover and the ChemCam instrument are thanked for their part in this work. We also thank our reviewers, editor in chief, and Associate Editor for their useful and thoughtful comments that improved the manuscript. This work was supported by CNRS in France and by NASA's Mars Exploration Program in the US.

References

Agee, C. B., et al. (2013), Unique meteorite from early Amazonian Mars: Water-rich basaltic breccia Northwest Africa 7034, *Science*, *339*(6121), 780–785.

Anderson, R., et al. (2015), ChemCam results from the Shaler outcrop in Gale crater, Mars, *Icarus*, *249*, 2–21.

Barrat, J. A., A. Jambon, L. Ferrière, C. Bollinger, J. A. Langlade, C. Liorzou, O. Boudouma, and M. Fialin (2014), No Martian soil component in shergottite meteorites, *Geochim. Cosmochim. Acta*, *125*, 23–33.

Beck, P., et al. (2016), Carbon detection with ChemCam: Laboratory studies and Mars results, paper presented at 47th Lunar and Planet. Sci. Conf., Lunar Planet. Inst., The Woodlands, Tex.

Bilgin, B., G. Atun, and G. Keçeli (2001), Adsorption of strontium on illite, *J. Radioanal. Nucl. Chem.*, *250*(2), 323–328.

Brearley, A. J. (1998), Rare K-bearing mica in Allan Hills 84001: Additional constraints on carbonate formation, *LPI Contribution No 956*, 6, Houston, Tex.

Bridges, J. C., et al. (2016), Igneous differentiation on Mars: Trachybasalts in Gale crater, paper presented at 47th Lunar and Planet. Sci. Conf., Lunar Planet. Inst., The Woodlands, Tex.

Campbell, J. L. (2012), The instrumental blank of the Mars Science Laboratory alpha particle X-ray spectrometer, *Nucl. Instrum. Methods Phys. Res. Sect. B*, *288*, 102–110.
Clegg, S. M., et al. (2017), Recalibration of the Mars Science Laboratory ChemCam instrument with an expanded geochemical database, *Spectrochim. Acta, Part B*, *129*, 64–85.
Cousin, A., O. Forni, S. Maurice, O. Gasnault, C. Fabre, V. Sautter, R. C. Wiens, and J. Mazoyera (2011), Laser induced breakdown spectroscopy library for the Martian environment, *Spectrochim. Acta, Part B*, *66*(11), 805–814.
Cousin, A., et al. (2014), Chemistry of coarse particles in soils and their relationship with local rocks, paper presented at 8th Int. Conf. on Mars, LPI Contributions, 1791, 1095, Pasadena, Calif.
Cousin, A., et al. (2015), Igneous rock classification at Gale (sols 13–800), paper presented at 46th Lunar and Planet. Sci. Conf., Lunar Planet. Inst., The Woodlands, Tex.
Cousin, C., et al. (2017). Classification of igneous rocks analyzed by ChemCam at Gale Crater, Mars. *Icarus*, doi:10.1016/j.icarus.2017.01.014, in press.
Cremers, D. A., and L. J. Radziemski (2006), Basics of the LIBS plasma, in *Handbook of Laser-Induced Breakdown Spectroscopy*, pp. 23–52, John Wiley, Hoboken, N. J.
Deer, W. A., R. A. Howie, and J. Zussman (Eds.) (2001), Feldspars, in *An Introduction to the Rock-forming Minerals*, vol. 4A, Mineralogical Society of Great Britain & Ireland, London, U. K.
Elliott, J. C. (1994), *Structure and Chemistry of the Apatites and Other Calcium Orthophosphates*, vol. 18, Elsevier, Amsterdam, Netherlands.
Eppler, A. S., D. A. Cremers, D. D. Hickmott, M. J. Ferris, and A. C. Koskelo (1996), Matrix effects in the detection of Pb and Ba in soils using laser-induced breakdown spectroscopy, *Appl. Spectrosc.*, *50*(9), 1175–1181.
Essington, M. E., G. V. Melnichenko, M. A. Stewart, and R. A. Hull (2009), Soil metals analysis using laser-induced breakdown spectroscopy (LIBS), *Soil Sci. Soc. Am. J.*, *73*(5), 1469–1478.
Fabre, C., M. C. Boiron, J. Dubessy, A. Chabiron, B. Charoy, and T. M. Crespo (2002), Advances in lithium analysis in solids by means of laser-induced breakdown spectroscopy: An exploratory study, *Geochim. Cosmochim. Acta*, *66*(8), 1401–1407.
Fabre, C., S. Maurice, A. Cousin, R. C. Wiens, O. Forni, V. Sautter, and D. Guillaume (2011), Onboard calibration igneous targets for the Mars Science Laboratory Curiosity rover and the Chemistry Camera laser induced breakdown spectroscopy instrument, *Spectrochim. Acta, Part B*, *66*(3), 280–289.
Fabre, C., et al. (2014), In situ calibration using univariate analyses based on the onboard ChemCam targets: First prediction of Martian rock and soil compositions, *Spectrochim. Acta, Part B*, *99*, 34–51.
Farley, K. A., et al. (2014), In situ radiometric and exposure age dating of the Martian surface, *Science*, *343*(6169, 1247166).
Forni, O., et al. (2015), First detection of fluorine on Mars: Implications for Gale Crater's geochemistry, *Geophys. Res. Lett.*, *42*, 1020–1028, doi:10.1002/2014GL062742.
Foster, M. D. (1960), *Interpretation of the Composition of Lithium Micas*, vol. 354-E, pp. 115–147, U.S. Geol. Surv. Prof. Pap., Washington, D. C.
Grotzinger, J. P., et al. (2015), Deposition, exhumation, and paleoclimate of an ancient lake deposit, Gale crater, Mars, *Science*, *350*(6257), aac7575.
Hark, R. R., and R. S. Harmon (2014), Geochemical fingerprinting using LIBS, in *Laser-Induced Breakdown Spectroscopy*, pp. 309–348, Springer, Berlin.
Heier, K. S., and G. K. Billings (1970), Rubidium, in *Handbook of Geochemistry*, vol. 2, pp. 2, Springer, Berlin.
Hewins, R. H., et al. (2017), Regolith breccia Northwest Africa 7533: Mineralogy and petrology with implications for early Mars, *Meteorit. Planet. Sci.*, *52*(1), 89–124.
Humayun, M., et al. (2013), Origin and age of the earliest Martian crust from meteorite NWA [thinsp] 7533, *Nature*, *503*(7477), 513–516.
Johnson, M. C., M. J. Rutherford, and P. C. Hess (1991), Chassigny petrogenesis: Melt compositions, intensive parameters and water contents of Martian (?) magmas, *Geochim. Cosmochim. Acta*, *55*(1), 349–366.
Kabata, A., and H. Pendias (2010), *Trace Elements in Soils and Plants*, CRC, Boca Raton, Fla.
Kogel, J. E. (Ed) (2006), *Industrial Minerals & Rocks: Commodities, Markets, and Uses*, SME, Littleton, Colo.
Lanza, N. L., et al. (2015), Understanding the signature of rock coatings in laser-induced breakdown spectroscopy data, *Icarus*, *249*, 62–73.
Lanza, N. L., et al. (2016), Oxidation of manganese in an ancient aquifer, Kimberley formation, Gale crater, Mars, *Geophys. Res. Lett.*, *43*, 7398–7407, doi:10.1002/2016GL069109.
Lasue, J., R. C. Wiens, S. M. Clegg, D. T. Vaniman, K. H. Joy, S. Humphries, A. Mezzacappa, N. Melikechi, R. E. McInroy, and S. Bender (2012), Remote laser-induced breakdown spectroscopy (LIBS) for lunar exploration, *J. Geophys. Res.*, *117*, E01002, doi:10.1029/2011JE003898.
Lasue, J., et al. (2016), Observation of $>$5 wt% zinc at the Kimberley outcrop, Gale crater, Mars, *J. Geophys. Res. Planets*, *121*, 338–352, doi:10.1002/2015JE004946.
Le Deit, L., et al. (2016), The potassic sedimentary rocks in Gale Crater, Mars, as seen by ChemCam on board Curiosity, *J. Geophys. Res. Planets*, *121*, 784–804, doi:10.1002/2015JE004987.
Le Mouélic, S., et al. (2015), The ChemCam Remote Micro-Imager at Gale crater: Review of the first year of operations on Mars, *Icarus*, *249*, 93–107.
Léveillé, R. J., et al. (2014), Chemistry of fracture-filling raised ridges in Yellowknife Bay, Gale Crater: Window into past aqueous activity and habitability on Mars, *J. Geophys. Res. Planets*, *119*, 2398–2415, doi:10.1002/2014JE004620.
Lyons, W. B., and K. A. Welch (1997), Lithium in waters of a polar desert, *Geochim. Cosmochim. Acta*, *61*(20), 4309–4319.
Mansoori, A., B. Roshanzadeh, M. Khalaji, and S. H. Tavassoli (2011), Quantitative analysis of cement powder by laser induced breakdown spectroscopy, *Opt. Lasers Eng.*, *49*(3), 318–323.
Martin, M. Z., S. Allman, D. J. Brice, R. C. Martin, and N. O. Andre (2012), Exploring laser-induced breakdown spectroscopy for nuclear materials analysis and in-situ applications, *Spectrochim. Acta, Part B*, *74*, 177–183.
Maurice, S., et al. (2012), The ChemCam instrument suite on the Mars Science Laboratory (MSL) rover: Science objectives and mast unit description, *Space Sci. Rev.*, *170*(1–4), 95–166.
Maurice, S., et al. (2016), ChemCam activities and discoveries during the nominal mission of the Mars Science Laboratory in Gale crater, Mars, *J. Anal. At. Spectrom.*, *31*(4), 863–889.
McLennan, S. M., et al. (2014), Elemental geochemistry of sedimentary rocks at Yellowknife Bay, Gale crater, Mars, *Science*, *343*(6169, 1244734).
Meslin, P. Y., et al. (2013), Soil diversity and hydration as observed by ChemCam at Gale Crater, Mars, *Science*, *341*(6153), 1,238,670.
Meslin, P. Y., et al. (2016), Calibration of the fluorine, chlorine, and hydrogen content of apatites with the ChemCam LIBS instrument, presented at 47th Lunar and Planetary Science Conference, Lunar Planetary Institute, The Woodlands, Tex.
Meyer, C. (2015), *The Martian Meteorite Compendium*, Astromaterials Research & Exploration Science (ARES). [Available at http://curator.jsc.nasa.gov/antmet/mmc/.]

Millot, G. (2013), *Geology of Clays: Weathering, Sedimentology, Geochemistry*, Springer Science & Business Media, Berlin.
Miziolek, A. W., V. Palleschi, and I. Schechter (Eds.) (2006), *Laser Induced Breakdown Spectroscopy*, Cambridge Univ. Press, Cambridge, U. K.
Nachon, M., et al. (2014), Calcium sulfate veins characterized by ChemCam/Curiosity at Gale crater, Mars, *J. Geophys. Res. Planets*, *119*, 1991–2016, doi:10.1002/2013JE004588.
Nachon, M., et al. (2016), Chemistry of diagenetic features analyzed by ChemCam at Pahrump Hills, Gale crater, Mars, *Icarus*, *281*, 121–136.
Nyquist, L. E., D. D. Bogard, C. Y. Shih, A. Greshake, D. Stöffler, and O. Eugster (2001), Ages and geologic histories of Martian meteorites, in *Chronology and Evolution of Mars*, pp. 105–164, Springer, Netherlands.
Nyquist, L. E., C.-Y. Shih, F. M. McCubbin, A. R. Santos, C. K. Shearer, Z. X. Peng, P. V. Burger, and C. B. Agee (2016), Rb-Sr and Sm-Nd isotopic and REE studies of igneous components in the bulk matrix domain of Martian breccia Northwest Africa 7034, *Meteorit. Planet. Sci.*, *51*, 483–498.
Ollila, A. M., et al. (2014), Trace element geochemistry (Li, Ba, Sr, and Rb) using Curiosity's ChemCam: Early results for Gale crater from Bradbury landing site to Rocknest, *J. Geophys. Res. Planets*, *119*, 255–285, doi:10.1002/2013JE004517.
Palucis, M. C., W. E. Dietrich, A. G. Hayes, R. M. E. Williams, S. Gupta, N. Mangold, H. Newsom, C. Hardgrove, F. Calef III, and D. Y. Sumner (2014), The origin and evolution of the Peace Vallis fan system that drains to the Curiosity landing area, Gale Crater, Mars, *J. Geophys. Res. Planets*, *119*, 705–728, doi:10.1002/2013JE004583.
Payré, V., et al. (2016), Copper abundances in Gale Crater: First ChemCam calibration and quantification, paper presented at 47th Lunar and Planet. Sci. Conf., Lunar Planet. Inst., The Woodlands, Tex.
Rao, M. N., L. E. Borg, D. S. McKay, and S. J. Wentworth (1999), Martian soil component in impact glasses in a Martian meteorite, *Geophys. Res. Lett.*, *26*(21), 3265–3268, doi:10.1029/1999GL005388.
Rapin, W., et al. (2016), Hydration state of calcium sulfates in Gale crater, Mars: Identification of bassanite veins, *Earth Planet. Sci. Lett.*, *452*, 197–205.
Sautter, V., et al. (2014), Igneous mineralogy at Bradbury Rise: The first ChemCam campaign at Gale crater, *J. Geophys. Res. Planets*, *119*, 30–46, doi:10.1002/2013JE004472.
Sautter, V., et al. (2015), In situ evidence for continental crust on early Mars, *Nat. Geosci.*, *8*(8), 605–609.
Sautter, V., et al. (2016), Magmatic complexity on early Mars as seen through a combination of orbital, in-situ and meteorite data, *Lithos*, *254*, 36–52.
Schröder, S., et al. (2015), Hydrogen detection with ChemCam at Gale crater, *Icarus*, *249*, 43–61.
Shibata, T., G. Thompson, and F. A. Frey (1979), Tholeiitic and alkali basalts from the Mid-Atlantic Ridge at 43 N, *Contrib. Mineral. Petrol.*, *70*(2), 127–141.
Short, N. M. (1961), Geochemical variations in four residual soils, *J. Geol.*, *69*(5), 534–571.
Simmons, E. C. (1999), Strontium: Element and Geochemistry, in *Encyclopedia of Geochemistry*, edited by C. P. Marschall and R. W. Fairbridge, pp. 598–599, Kluwer Acad., Dordrecht, Netherlands.
Stolper, E. M., et al. (2013), The petrochemistry of Jake_M: A Martian mugearite, *Science*, *341*(6153, 1239463).
Stubblefield, C. B., and R. O. Bach (1972), Solubility of lithium fluoride in water, *J. Chem. Eng. Data*, *17*(4), 491–492.
Sweetapple, M. T., and S. Tassios (2015), Laser-induced breakdown spectroscopy (LIBS) as a tool for in situ mapping and textural interpretation of lithium in pegmatite minerals, *Am. Mineral.*, *100*(10), 2141–2151.
Tanaka, K. L., S. J. Robbins, C. M. Fortezzo, J. A. Skinner, and T. M. Hare (2014), The digital global geologic map of Mars: Chronostratigraphic ages, topographic and crater morphologic characteristics, and updated resurfacing history, *Planet. Space Sci.*, *95*, 11–24.
Taylor, S. R., and S. McLennan (2009), *Planetary Crusts: Their Composition, Origin and Evolution*, Cambridge Univ. Press, Cambridge, U. K.
Treiman, A. H., et al. (2016), Mineralogy, provenance, and diagenesis of a potassic basaltic sandstone on Mars: CheMin X-ray diffraction of the Windjana sample (Kimberley area, Gale Crater), *J. Geophys. Res. Planets*, *121*, 75–106, doi:10.1002/2015JE004932.
Ure, A., and M. Berrow (1982), Chapter 3. The elemental constituents of soils, in *Environmental Chemistry. Royal Society of Chemistry*, edited by H. J. M. Bowen, pp. 94–203, London, U. K.
Vaniman, D., M. D. Dyar, R. Wiens, A. Ollila, N. Lanza, J. Lasue, J. M. Rhodes, S. Clegg, and H. Newsom (2012), Ceramic ChemCam calibration targets on Mars science laboratory, *Space Sci. Rev.*, *170*(1–4), 229–255.
Wedepohl, K. H. (1978), *Handbook of Geochemistry*, vol. 11, Springer, Berlin.
Wiens, R. C., et al. (2012), The ChemCam instrument suite on the Mars Science Laboratory (MSL) rover: Body unit and combined system tests, *Space Sci. Rev.*, *170*(1–4), 167–227.
Wiens, R. C., et al. (2013), Pre-flight calibration and initial data processing for the ChemCam laser-induced breakdown spectroscopy instrument on the Mars Science Laboratory rover, *Spectrochim. Acta, Part B*, *82*, 1–27.
Wiens, R. C., et al. (2015), Major-element compositional diversity observed by ChemCam along the MSL traverse: The first three years, paper presented at 2015 Fall Meeting, AGU, San Francisco, Calif.
Wittmann, A., R. L. Korotev, B. L. Jolliff, A. J. Irving, D. E. Moser, I. Barker, and D. Rumble (2015), Petrography and composition of Martian regolith breccia meteorite Northwest Africa 7475, *Meteorit. Planet. Sci.*, *50*(2), 326–352.